J. Mech. Phys. Solids 164 (2022) 104873

Contents lists available at ScienceDirect

Journal of the Mechanics and Physics of Solids

journal homepage: www.elsevier.com/locate/jmps

Ductile failure predictions using micromechanically-based computational models

Lars Edvard Blystad Dæhli [a,*], Cihan Tekoğlu [b], David Morin [a,c], Tore Børvik [a,c], Odd Sture Hopperstad [a,c]

[a] Structural Impact Laboratory (SIMLab), Department of Structural Engineering, NTNU – Norwegian University of Science and Technology, NO-7491, Trondheim, Norway
[b] Department of Mechanical Engineering, TOBB University of Economics and Technology, Söğütözü, Ankara, 06560, Turkey
[c] Centre for Advanced Structural Analysis (CASA), Department of Structural Engineering, NTNU – Norwegian University of Science and Technology, NO 7491, Trondheim Norway

ARTICLE INFO

Keywords:
Strain localization
Void coalescence
Ductile fracture
Micromechanical modelling
Unit cell model
Finite element analysis

ABSTRACT

Three different micromechanically-based computational models for fracture in porous ductile solids are compared and assessed. Model A is a unit cell model of a porous ductile solid comprising a uniform periodic distribution of voids subjected to normal macroscopic loading. Models B and C, on the other hand, are unit-cell type models that represent an imperfection band governed by a doubly periodic array of voids separating two non-porous outer blocks. The outer blocks have a finite size in Model B and are semi-infinite in Model C. The non-porous material surrounding the voids, and the material of the outer blocks in Model B and Model C, are considered as an elasto-plastic isotropic material. Numerical simulations are performed for a wide range of macroscopic stress states. For each model, various criteria for determining the onset of ductile failure are evaluated to demonstrate their impact on the failure predictions. The results show that the failure loci strongly depend on the computational model and failure criterion employed. Thus, these three models cannot be used interchangeably – neither to investigate failure mechanisms nor to develop or calibrate fracture models – and an unambiguous failure criterion must be chosen.

1. Introduction

Structural metals often fail in a ductile manner. Although several mechanisms may be active in the ductile failure process (Noell et al., 2018), a commonly observed mechanism is transgranular fracture due to nucleation, growth, and coalescence of microscopic voids, where voids nucleate either by decohesion or cracking of intermetallic particles (Tipper, 1949; Rogers, 1960; Gurland and Plateau, 1963; Garrison and Moody, 1987). The ductile failure process can occur in various ways, which can broadly be categorized as localization-driven or coalescence-driven (see e.g. Tekoğlu et al. (2015) or Pineau et al. (2016) for reference) depending on whether coalescence takes place subsequent to localization or not.

In the former category of mechanisms, localized deformation occurs first due to a mechanical instability or material imperfection, and ductile failure subsequently progresses within the localization bands. The localization may be preceded by material softening or be a mere consequence of heterogeneous plastic flow. This mechanism has been observed in studies by Morgeneyer et al. (2014, 2016, 2021) using advanced imaging techniques, and was well reproduced in finite element simulations adopting a crystal plasticity

* Corresponding author.
E-mail address: lars.e.dahli@ntnu.no (L.E.B. Dæhli).

https://doi.org/10.1016/j.jmps.2022.104873
Received 13 October 2021; Received in revised form 28 January 2022; Accepted 18 March 2022
Available online 31 March 2022

constitutive model (Morgeneyer et al., 2021) that allows for heterogeneous material properties in the numerical model. A detailed numerical study on this type of mechanism was undertaken by Tekoğlu et al. (2015). Their work, based on a finite element model of the imperfection band analysis formulated by Rice (1976), shows that strain localization either precedes, or takes place at the same time, as void coalescence depending upon the stress triaxiality.

In the latter category of mechanisms, strain localization is caused by void coalescence and thus occurs after the material has started to soften due to void growth. This type of mechanism can be observed e.g. in studies by Babout et al. (2004), Weck et al. (2008), and Maire et al. (2011) using *in situ* imaging techniques. It was also discussed in the study by Vishwakarma and Keralavarma (2019) whose numerical analyses based on a multi-surface plasticity model (Keralavarma, 2017) indicate that strain localization could be initiated by void coalescence.

The underlying failure mechanisms must be properly accounted for in the micromechanical models in order to obtain reliable results and to facilitate development of predictive damage and failure models for large-scale applications. Since the seminal work of Needleman (1972), which gave the first detailed account of the interaction between neighbouring voids using finite element unit cell analyses, numerical modelling and simulations have been instrumental for expanding the knowledge regarding the underlying mechanisms of ductile fracture in metal alloys. A large body of literature is devoted to examining the influence of various mechanical quantities and microstructural features on the microstructural evolution and predictions of material failure. For a detailed list of references, we refer to the comprehensive reviews by Benzerga and Leblond (2010), Benzerga et al. (2016) and Pineau et al. (2016).

A general conclusion from such micromechanically-based numerical studies, which support observations from earlier experimental work (e.g. Clausing (1970), Mackenzie et al. (1977), Hancock and Brown (1983), Thomson and Hancock (1984) and Bao and Wierzbicki (2004)), is that the stress state has a large influence on the material's ductility. More specifically, unit cell simulations show that the failure strain, usually associated with some material instability reflected by the model, decreases with the stress triaxiality ratio (e.g. Koplik and Needleman (1988), Kim et al. (2004), Gao and Kim (2006)) and varies greatly with the Lode parameter for low and intermediate values of the stress triaxiality ratio (e.g. Barsoum and Faleskog (2007, 2011) and Dunand and Mohr (2014)). This stress state dependence also provides an explanation for the non-monotonic appearance of the fracture locus in plane stress observed by e.g. Bao and Wierzbicki (2004), which arises due to the simultaneous change of the stress triaxiality and the Lode parameter when the admissible states of plane stress are traversed. Further, unit cells subjected to non-proportional loading (e.g. Benzerga et al. (2012) and Dæhli et al. (2016)) have shown that the fracture loci derived from micromechanical analyses are generally path dependent and not intrinsic to the material.

In addition to being a valuable tool for mechanism-based studies, micromechanical simulations have also been utilized to calibrate and develop ductile fracture models and porous plasticity models (e.g. Koplik and Needleman (1988), Faleskog et al. (1998), Steglich et al. (2010), Brünig et al. (2013), Bomarito and Warner (2015) and Dæhli et al. (2018)). A caveat with respect to such procedures is that the results depend on the computational model that is applied. While the effect of stress triaxiality is consistent, it seems that the influence of the Lode parameter on ductility observed in micromechanical studies has not been fully elucidated. For instance, the unit cell simulations conducted by Yu et al. (2016) and Dæhli et al. (2018) display a monotonic increase of the failure strain with respect to the Lode parameter, while those performed by Barsoum and Faleskog (2007, 2011), Dunand and Mohr (2014), and Dæhli et al. (2017b) display a non-monotonic fracture locus that usually exhibit a minimum ductility for shear-dominated stress states. This discrepancy is rooted in the underlying formulation of the computational models used in the different studies.

Since most numerical studies have been based on unit cell models, i.e. models where the distribution of voids (or particles) is assumed to be uniform, the boundary conditions have a major impact on the results. More recently, Cadet et al. (2021) have performed numerical simulations based on representative volume elements containing many voids. This facilitates a representation of the complex interplay between voids that invariably takes place in real materials. Their analyses show that the fracture locus is very sensitive to the spatial void distribution. Further, a non-monotonic fracture locus with respect to the Lode parameter was obtained even when a macroscopic normal stress state was imposed to the model, i.e. no macroscopic shear stresses were permitted. This result is in contrast to unit cell models subjected to similar boundary conditions.

A key motivation for the current work is to highlight the differences between the numerical predictions of three micromechanical models that are all relevant in the context of porous ductile solids. The study is focussed on unit cell models, since these are used in the majority of previous studies in the literature. We use identical material properties in the various computational models and impose a range of loading conditions to elucidate their differences. The results demonstrate that the similarities between the predictions depend on several aspects, such as the adopted failure criterion and the imposed macroscopic loading. The failure loci for the three models are rather similar when the Lode parameter is kept constant. However, the influence of the Lode parameter on the predicted failure loci depends upon the adopted micromechanical model and the measure used to predict failure.

The paper is organized as follows. Section 2 provides the scope and overview of the work. Section 3 includes a short presentation of the matrix constitutive model and a description of the three micromechanical models used throughout the study. Results and discussion are found in Section 4, while Section 5 presents some concluding remarks.

2. Scope and overview

In this work, we utilize three different micromechanically-based finite element models to examine the ductile failure of an aluminium alloy. We assume that the material initially contains voids and disregard any effects associated with the presence of a particle. This assumption is justified for materials with loosely bonded particles subjected to intermediate and high stress triaxiality ratios, for which void nucleation occurs at small deformations (see e.g. Tekoğlu and Pardoen, 2010, and the references therein). An overview of the computational models is shown in Fig. 1.

From left-to-right, the schematics in Fig. 1 represent:

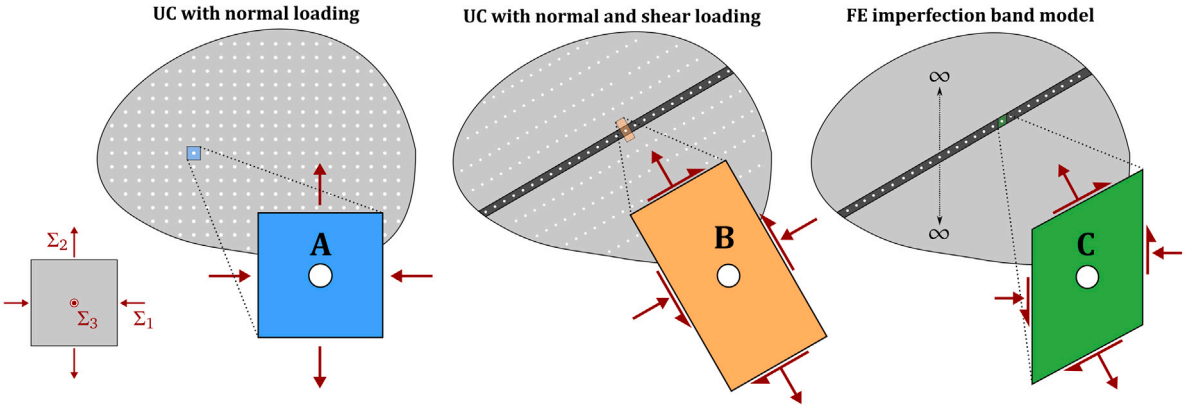

Fig. 1. Overview of three computational models for micromechanical studies of ductile fracture. Model A corresponds to a unit cell for an idealized material containing a uniform, triply periodic void distribution; the unit cell is subjected only to normal loads. Model C is an FE implementation of the imperfection band model of Rice (1976), where a thin planar band containing a doubly periodic array of voids lies between two semi-infinite outer blocks made of the same non-porous material. Finally, Model B can be viewed either as a version of Model A where the unit cell is subjected to normal and shear loads or a version of Model C with finite-size outer blocks.

A. a voided unit cell model subjected to normal loads (blue),
B. an imperfection band analysis model – with *finite-sized* outer blocks separated by the band – subjected to normal and shear loads (orange),
C. an imperfection band analysis model – with *semi-infinite* outer blocks separated by the band – subjected to normal and shear loads (green).

The computational models are based on idealistic descriptions of the material microstructure, represented by voids that are either embedded within a homogeneous matrix or situated within a thin planar imperfection band. These models are used to various extent in conjunction with micromechanical modelling of ductile fracture, but they often serve similar purposes: to undertake mechanism-based studies of ductile fracture, to derive failure loci and make ductile fracture assessments, and to calibrate ductile fracture models. However, these models differ in various ways and their predictions cannot *a priori* be assumed to coincide neither quantitatively nor qualitatively. Some key differences and characteristics of the three models can be briefly summarized as:

- Model A considers only normal loading components and is consequently restricted to scenarios where void coalescence takes place on planes that are normal to the major principal loading direction, i.e. a normal coalescence mode corresponding to void coalescence by internal necking. This type of model is frequently employed in the literature (see e.g. Brünig et al. (2013), Liu et al. (2016), Yu et al. (2016), Dæhli et al. (2018) and Frodal et al. (2019)), which serves as the key motivation for including it herein although it is quite restrictive in terms of possible failure modes.
- Models B and C account for a shear deformation mode that facilitates void rotation and shearing, and thus enable a description of strain localization and void coalescence in directions that are rotated with respect to the principal loading axes. These two models represent similar failure mechanisms, but differ in the imposed boundary conditions and unit cell geometry.
- Model B can be viewed in two ways: either as (i) a version of the imperfection band analysis with *finite-size* outer blocks separated by the band, or (ii) a unit cell model for a ductile material containing a triply periodic void distribution, subjected to a stress state that includes three normal and one shear loading components. The latter view is conceptually similar to Model A, but allows for void shearing and rotation that has a marked influence on the macroscopic response of the unit cell. Note that this hints at Model A being a restricted version of Model B, as also discussed in Section 3.3.
- Model C is a detailed FE implementation of the imperfection band model (Rice, 1976) and describes a uniform, non-porous, and isotropic material subjected to a homogeneous deformation that fails due to strain localization within an infinitesimal planar imperfection band. In this sense, the porosity of the material is zero although the imperfection band is explicitly modelled with a non-zero void volume fraction, and the material would appear to fail by sudden localization of deformation for an external observer probing the macroscopic response.

Due to these inherent differences, we believe it is essential to compare these three models and assess their predictive capabilities in terms of both macroscopic material response and ductile failure.

3. Numerical modelling

3.1. Matrix constitutive model

An extruded AA6063-T6 aluminium alloy recently characterized by Thomesen et al. (2021) is used to describe the matrix behaviour. The inherent plastic anisotropy due to extrusion is disregarded in this study, and the material test data is merely used

Table 1
Overview of the material parameters used for matrix behaviour.

E [GPa]	ν	σ_0 [MPa]	Q_1 [MPa]	C_1	Q_2 [MPa]	C_2	f_0
70	0.3	221.7	54.3	35.4	36.1	0.77	0.0063

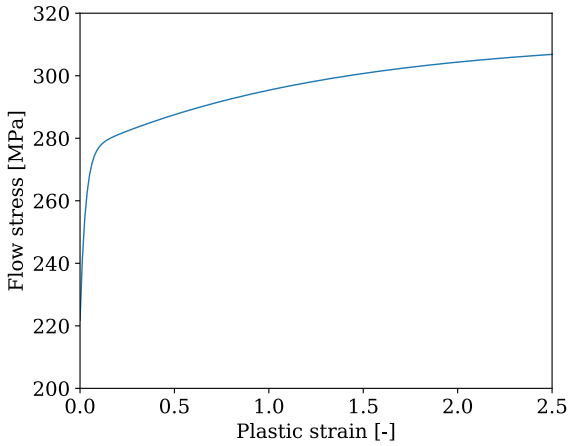

Fig. 2. Matrix flow stress as a function of the accumulated plastic strain. The material parameters pertain to an AA6063-T6 aluminium alloy, see Table 1.

to impose relevant material properties in the numerical simulations. The alloy's particle area fraction is used as a reference value for the initial porosity (f_0), see Table 1.

The matrix is modelled as an elasto-plastic solid based on the J_2 flow theory with a hypoelastic formulation of the generalized Hooke's law and an extended Voce hardening rule. The flow stress of the material is given by

$$\sigma_{\mathrm{M}} = \sigma_0 + \sum_{i=1}^{2} Q_i \Big(1 - \exp\big(-C_i p\big)\Big) \tag{1}$$

where p is the accumulated plastic strain, σ_0 is the yield stress, and Q_i and C_i are the work hardening parameters. Material parameters governing the matrix behaviour and the initial porosity are listed in Table 1 and the resulting matrix flow stress curve is shown in Fig. 2. We have utilized the built-in material model of Abaqus/Standard in all the simulations, while a UHARD user subroutine is used to update the matrix flow stress throughout the numerical simulations.

3.2. Macroscopic loading conditions

The macroscopic loading is defined in terms of stress state parameters that are evaluated from the macroscopic Cauchy stress tensor ($\boldsymbol{\Sigma}$). In the sequel, we refer to the stress triaxiality ratio (T) and the Lode parameter (L):

$$T = \frac{\Sigma_{\mathrm{I}} + \Sigma_{\mathrm{II}} + \Sigma_{\mathrm{III}}}{3\Sigma_{\mathrm{eq}}}, \quad L = \frac{2\Sigma_{\mathrm{II}} - \Sigma_{\mathrm{I}} - \Sigma_{\mathrm{III}}}{\Sigma_{\mathrm{I}} - \Sigma_{\mathrm{III}}} \tag{2}$$

which have become standard stress state parameters in ductile fracture models. In Eq. (2), Σ_{eq} is the macroscopic von Mises equivalent stress and $\Sigma_{\mathrm{I}} \geq \Sigma_{\mathrm{II}} \geq \Sigma_{\mathrm{III}}$ are the ordered principal values of the macroscopic stress tensor. The Lode parameter yields stress states of generalized tension for $L = -1$, generalized shear for $L = 0$, and generalized compression/biaxial tension for $L = 1$.

The three computational models are subjected to various states of macroscopic proportional loading to elucidate the differences between them. To examine the effects of the hydrostatic stress, we have imposed stress triaxiality ratios corresponding to $T = \{0.6,\ 0.75,\ 1.0,\ 1.5,\ 2.0\}$ for $L = -1$. Further, the effects of the deviatoric stress are examined by imposing $T = \{0.75,\ 2.0\}$ for $L = \{-1, -1/2, 0, 1/2, 1\}$.

3.3. Model A – a voided unit cell model subjected to normal loads

The modelling framework for Model A corresponds to a triply periodic stacking of voids subjected to loading conditions governed by macroscopic normal stress components. This type of unit cell models are widely used for micromechanically-based studies in the literature (see e.g. Needleman (1972), Koplik and Needleman (1988), Becker et al. (1989), Kuna and Sun (1996), Søvik and Thaulow (1997), Zhang et al. (2001), Kim et al. (2004), Gao and Kim (2006), Lin et al. (2006), Steglich et al. (2008), Gao et al. (2010), Steglich et al. (2010), Yerra et al. (2010), Keralavarma et al. (2011), Lecarme et al. (2011), Benzerga et al. (2012), Dæhli et al. (2016), Kristoffersen et al. (2016), Shinohara et al. (2016), Yu et al. (2016), Frodal et al. (2019) and Morin et al. (2019)). An illustration of the modelling framework and the meshed FE model are shown in Fig. 3. Note that the boundary conditions imposed in

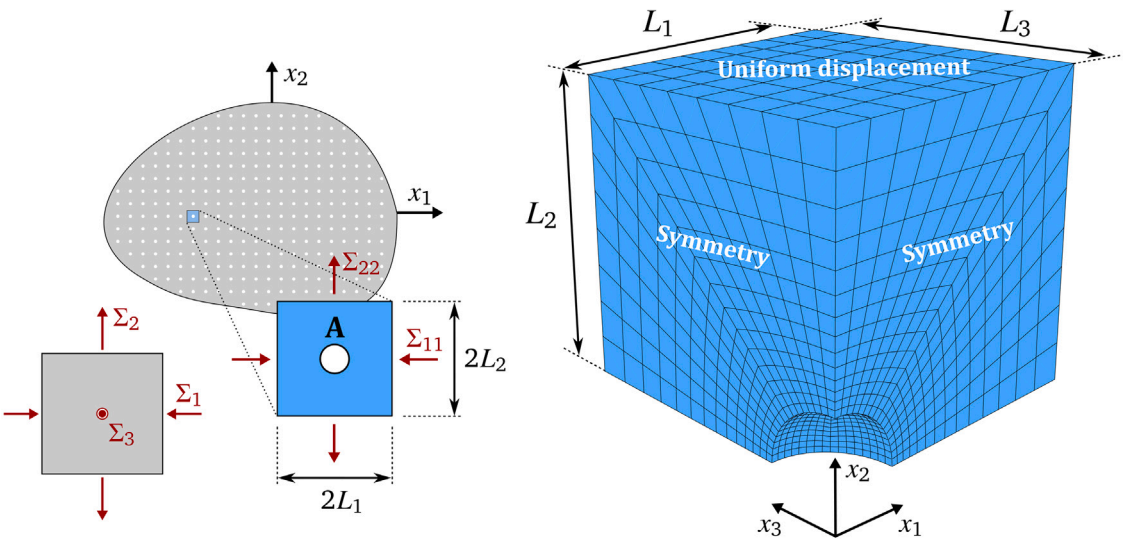

Fig. 3. Model A. Illustration of the unit cell model and the associated 3D FE model. A 2D view is shown to the left to aid the interpretation of the various quantities associated with the model. The FE model corresponds to a cube cut out from a triply periodic arrangement of equally-spaced spherical voids. As only normal stresses are imposed on the unit cell in Model A, the triply periodic void distribution is accounted for by employing a one-eighth unit cell model whose external surfaces are kept straight and parallel to their original planes during the entire loading.

Model A preclude shear localization and failure is consequently restricted to occur by internal necking driven by the tensile stresses, i.e. a normal coalescence mode. It can be questioned whether these simplified boundary conditions are appropriate for general three-dimensional loading cases, but similar models are still used in several studies of recent date, which is the key motivation for including it in the current study.

The initial geometry comprises a cube with dimensions $2L_1 = 2L_2 = 2L_3 = \bar{L}$ and a spherical, centred void with radius R. The void spacing is thus equal in all directions, and the initial void volume fraction of the unit cell is given by $f_0 = 4\pi R^3/3\bar{L}^3$ and corresponds to the value listed in Table 1. We further assume that the unit cell, and thus the stacking direction of the voids, is aligned with the macroscopic principal stress directions such that the unit cell is loaded by macroscopic normal stress components (Σ_i). As only normal stresses are imposed, the triply periodic void distribution is accounted for by employing a one-eighth unit cell model whose external surfaces are kept straight and parallel to their original planes during the entire loading. Based on a mesh convergence study conducted on beforehand, we used an FE mesh that contains approximately 3000 linear solid elements with selectively reduced integration (C3D8) in the numerical simulations. This mesh density corresponds to that used in the central part of Model B in order to achieve the same level of accuracy.

The ratios between the macroscopic stress components are kept at fixed values, such that the unit cell is subjected to macroscopically proportional loading governed by the constant values of T and L listed in Section 3.2. The loading control is enforced by nonlinear multi-point constraints implemented as an MPC user subroutine in the implicit FE solver Abaqus/Standard. Details of this procedure have been presented elsewhere (see e.g. Faleskog et al. (1998), Cheng and Guo (2007), Dæhli et al. (2016), Liu et al. (2016), Dæhli et al. (2017a)) and will not be repeated here.

3.4. Model B – an imperfection band analysis model with finite-sized outer blocks

The modelling framework for Model B was presented in detail by Dæhli et al. (2017b) and closely follows the work of Barsoum and Faleskog (2007, 2011) and Dunand and Mohr (2014). Similar unit cell models have also been used in other studies related to micromechanical modelling of ductile fracture (e.g. Leblond and Mottet, 2008; Scheyvaerts et al., 2011; Tekoğlu, 2014; Bomarito and Warner, 2015; Wong and Guo, 2015; Bomarito and Warner, 2017; Guo and Wong, 2018; Zhu et al., 2018; Vishwakarma and Keralavarma, 2019). In a recent study, Luo and Gao (2018) have also assessed the effect of relaxing the material imperfection by including discrete voids of slightly smaller initial size in the outer blocks above and below the imperfection band. Fig. 4 provides an overview of Model B and an illustration of the FE model used in the numerical analyses.

The illustration to the left in Fig. 4 implies that the model can be viewed in two different ways:

- as an approximation to the imperfection band analysis of Rice (1976),
- as a unit cell cut out from a periodic material microstructure subjected to combined normal and shear loading.

The two main differences of Model B from the original analysis of Rice (1976) are that the outer blocks above and below the imperfection band are assumed to have a finite size, and the orientation of the imperfection band does not evolve during loading. That is, for a normal band where the orientation angle naturally remains $\Psi = \Psi_0 = 0°$ throughout the entire loading history, the

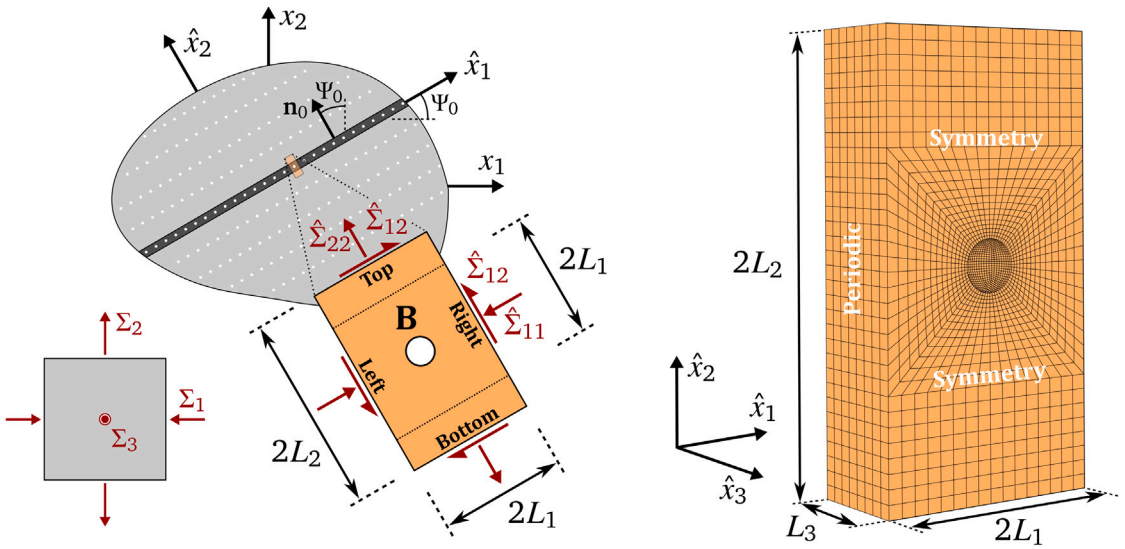

Fig. 4. Model B. Illustration of the imperfection band model with finite-sized outer blocks and the associated 3D FE model. A 2D view is shown to the left to aid the interpretation of the various quantities associated with the model. The FE model cuts through the imperfection band such that it encompasses the entire band region and extends some distance into the material outside the band. Zero shear tractions and normal displacement increments are applied to the surfaces of the FE model having a normal along the x_3-direction. The mid-plane cutting through the void is modelled as a symmetry plane, while a uniform displacement is applied to the back surface. Periodic boundary conditions (PBCs) are assigned between *Top* and *Bottom*, and *Right* and *Left* surfaces.

predictions of Model B converge to those of Rice's analysis as the ratio L_2/L_1 increases. In this regard, the first view seems to be the most natural interpretation when L_2 is notably larger than L_1, i.e. for slender unit cells, and is in line with the model used by e.g. Barsoum and Faleskog (2007, 2011) and Dunand and Mohr (2014). The second view is more in the spirit of Model A, but permits prescription of a macroscopic shear stress such that effects of void shearing on the mechanical response can be studied (see e.g. Leblond and Mottet (2008), Scheyvaerts et al. (2011), Tekoğlu (2014) and Bomarito and Warner (2015)). In the second view, varying the unit cell aspect ratio corresponds to changing the distance between neighbouring voids in different directions. Note that Model B reduces to Model A if the shear stress is specified to be zero and the unit cell dimensions are equal in all three directions. However, since unit cell models similar to Model A are widespread in the literature, we have chosen to treat it as an independent model herein.

The principal stress directions coincide with the coordinate axes x_i in such a way that $\Sigma_1 = \Sigma_{\mathrm{III}}$, $\Sigma_2 = \Sigma_{\mathrm{I}}$, and $\Sigma_3 = \Sigma_{\mathrm{II}}$. The fixed global coordinate system of the FE model is taken to coincide with the local coordinate system $\hat{x}_i$ that describes the band orientation, i.e. the FE model is aligned with the imperfection band. Further, we use an FE model that cuts through the hypothetical imperfection band such that it encompasses the entire band region and extends some distance into the material outside the band. The band region is represented by a cube with dimensions $\bar{L}\times\bar{L}\times\bar{L}$, where the band size $\bar{L}$ is defined such that $2L_1 = 2L_3 = \bar{L}$. The height is taken to be twice the width, i.e. $L_2 = 2L_1 = \bar{L}$. Thus, the initial unit cell geometry comprises a rectangular parallelepiped with a spherical void of radius R located at the centre, i.e. in the centre of the band region. To ensure conformity between the models, it is necessary to maintain the same size of the intervoid ligament in the various models. The initial void radius is thus determined by assuming that the void volume fraction listed in Table 1 applies to the band region, such that $f_0^{\mathrm{b}} = 4\pi R^3/3\bar{L}^3$.

Since strain localization takes place on material planes with a unit normal vector $\mathbf{n}$ that is perpendicular to the intermediate principal stress direction for isotropic materials (Rudnicki and Rice, 1975; Rice, 1976; Perrin and Leblond, 1993), we assume that $\hat{x}_3 = x_3$ and utilize this symmetry condition to model only half the unit cell, as shown in Fig. 4. The band orientation is then uniquely determined by the band angle Ψ_0 and the unit normal to the band is given by $\mathbf{n}_0 = [-\sin\Psi_0, \cos\Psi_0]^{\mathrm{T}}$. Note that the band angle is kept fixed in the numerical simulations to conform with previous studies (e.g. Barsoum and Faleskog (2007, 2011) and Wong and Guo (2015)). Zero shear tractions and normal displacement increments are applied to the symmetry planes of the band (i.e. the surfaces having a normal along the x_3-direction). The mid-plane cutting through the void is defined as a symmetry plane and consequently kept fixed in x_3-direction, while the back surface is subjected to a non-zero normal displacement. Periodic boundary conditions (PBCs) are assigned between *Top* and *Bottom*, and *Right* and *Left* surfaces, as indicated in Fig. 4.

With these modelling assumptions, the unit cell is subjected to four distinct macroscopic stress components: three normal components ($\hat{\Sigma}_{11}$, $\hat{\Sigma}_{22}$, $\hat{\Sigma}_{33} = \Sigma_3$) and one shear component ($\hat{\Sigma}_{12}$). Macroscopic proportional stress states governed by the values of T and L given in Section 3.2 are maintained throughout the analyses. The procedure for controlling the loading path is presented in Dæhli et al. (2017a) and only a brief summary will be given here. The ratios between the macroscopic principal stress components are defined by $\rho_{\mathrm{II}} = \Sigma_{\mathrm{II}}/\Sigma_{\mathrm{I}}$ and $\rho_{\mathrm{III}} = \Sigma_{\mathrm{III}}/\Sigma_{\mathrm{I}}$. The macroscopic stress components $\hat{\Sigma}_{ij}$ acting on the unit cell are then readily found from coordinate transformations, viz.

$$\hat{\Sigma}_{11} = \left(\sin^2\Psi_0 + \rho_{\mathrm{III}}\cos^2\Psi_0\right)\Sigma_{\mathrm{I}} \tag{3a}$$

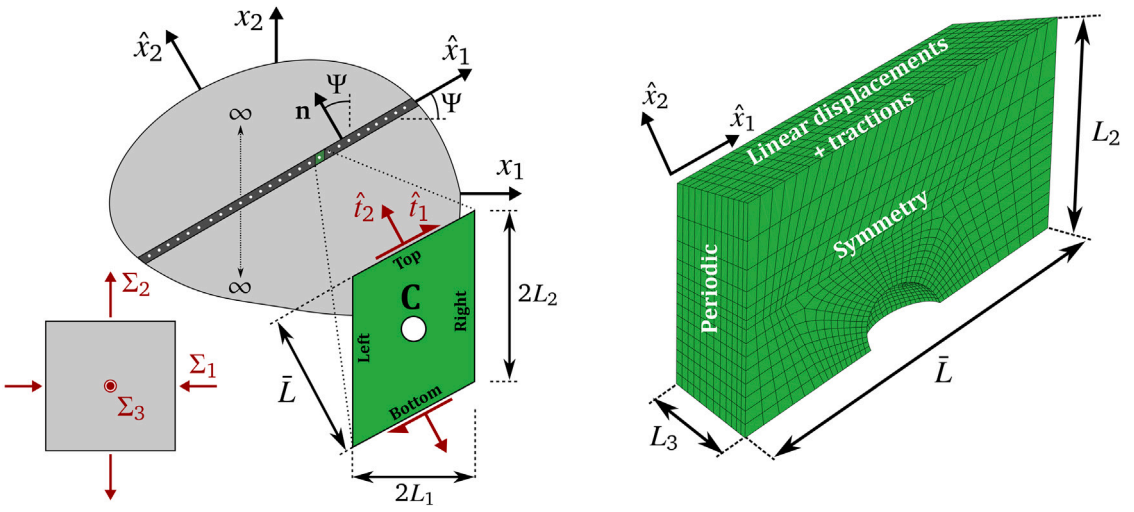

Fig. 5. Model C. Illustration of the imperfection band model and the associated 3D FE model. Owing to the doubly periodic void distribution in the band, the FE model is a parallelepiped with a spherical void at its centre. Boundary conditions are indicated on the surfaces of the FE mesh (right figure), apart from the mid-plane that lies parallel to the band, which is subjected to anti-symmetry conditions. A 2D view is shown to the left to aid the interpretation of the various quantities.

$$\hat{\Sigma}_{22} = \left(\cos^2 \Psi_0 + \rho_{\mathrm{III}} \sin^2 \Psi_0\right) \Sigma_{\mathrm{I}} \tag{3b}$$

$$\hat{\Sigma}_{33} = \rho_{\mathrm{II}} \Sigma_{\mathrm{I}} \tag{3c}$$

$$\hat{\Sigma}_{12} = \cos \Psi_0 \sin \Psi_0 \left(1 - \rho_{\mathrm{III}}\right) \Sigma_{\mathrm{I}} \tag{3d}$$

When the band orientation is assumed to be fixed, and with the ratios ρ_{II} and ρ_{III} being constant due to the macroscopically proportional loading paths, also the ratios between the macroscopic stress components $\hat{\Sigma}_{ij}$ remain constant. These loading conditions are enforced in the analyses by the use of non-linear kinematic constraints, which were implemented in an MPC user subroutine available in Abaqus/Standard (Barsoum and Faleskog, 2007, 2011; Dunand and Mohr, 2014; Wong and Guo, 2015; Dæhli et al., 2017a). Several band orientations Ψ_0 are imposed for each stress state, and the band orientation that gives the lowest strain to failure within an interval governed by $\Delta\Psi_0 = 1°$ is assumed to be critical and thus referred to as the critical orientation. As will become apparent from Section 4.2, failure can be defined in various ways in these numerical analyses, and the definition has implications for the results; it does not only affect the failure strain value itself, but also the critical orientation. To maintain coherence with Model C, we have chosen to define the critical orientation as the initial orientation with the lowest strain to localization. The numerical criterion for determining the onset of localization will be apparent from the discussion in Section 4.2. Only the results pertaining to the critical orientation will be presented and discussed in Section 4.

3.5. Model C – an imperfection band analysis model with semi-infinite outer blocks

The FE imperfection band model adopted here follows the work of Tekoğlu et al. (2015) and is a three-dimensional FE implementation of the general theory derived by Rice (1976). Similar models have been used by Tvergaard (1989) and Tvergaard (2015) in the case of plane strain and by Tvergaard and Legarth (2020) in a fully three-dimensional setting. Also, a version of the imperfection band model with finite-sized outer blocks was recently employed by Reboul et al. (2020) to study effects of strain rate sensitivity on strain localization. An illustration of the model and the corresponding FE model are shown in Fig. 5.

The imperfection band is placed within an infinite material block made from a homogeneous, non-porous material governed by the material properties compiled in Section 3.1 and contains a doubly periodic array of initially spherical voids. With reference to Fig. 5, we introduce a local coordinate system $\hat{x}_i$ that is attached to the band and follows the band rotation caused by deformation of the outer blocks above and below the band. A parallelepiped unit cell[1] is cut out from the band, as shown in Fig. 5. The initial void volume fraction within the band and the size of the intervoid ligament is identical to that used in Models A and B, which implies that the unit cell has height and width equal to $\bar{L}$ in the local coordinate system ($\hat{x}_i$). The initial width L_1 and initial height L_2 of the unit cell in the global coordinate system (x_i) depend upon the initial band orientation Ψ_0, viz.

$$2L_1 = \bar{L} \cos \Psi_0, \quad 2L_2 = \frac{\bar{L}}{\cos \Psi_0} \tag{4}$$

[1] Note that a rectangular unit cell aligned with the band could also have been used. Both types of model were used in the work of Tvergaard and Legarth (2020) and they were found to yield similar results.

Note that only 1/4 of the entire unit cell is modelled by the use of symmetry conditions on the front face and anti-symmetry conditions on the mid-plane defined by a cut through the void parallel to the band, respectively. The material outside the band is loaded along the principal stress axes (x_i) and subjected to macroscopic proportional loading governed by the constant values of T and L listed in Section 3.2. Strain and stress quantities outside the band are denoted E_i and Σ_i, respectively. Since the material is assumed to be isotropic, the imperfection band has unit normal vector $\mathbf{n}$ that is perpendicular to the intermediate principal stress direction (Rudnicki and Rice, 1975; Rice, 1976; Perrin and Leblond, 1993). In the model, we have chosen to align x_3 with the direction of the intermediate principal stress, i.e. $\Sigma_{\mathrm{II}} = \Sigma_3$ (with reference to Fig. 5). Further, we let x_1 and x_2 correspond to the directions of the minor and major principal stresses, such that $\Sigma_1 = \Sigma_{\mathrm{III}}$ and $\Sigma_2 = \Sigma_{\mathrm{I}}$. The main equations of the FE model will be presented next.

The unit normal to the band $\mathbf{n}$ (parallel to the $\hat{x}_2$-direction in Fig. 5) describes the current band orientation and evolves according to

$$\mathbf{n} = \frac{\mathbf{n}_0 \cdot \mathbf{F}^{-1}}{||\mathbf{n}_0 \cdot \mathbf{F}^{-1}||} \tag{5}$$

where $\mathbf{n}_0$ denotes the band normal in the initial configuration and $\mathbf{F}$ refers to the deformation gradient outside the band. The band normal $\mathbf{n}$ is uniquely defined by the band angle Ψ (see Fig. 5 for reference) through $\mathbf{n} = [-\sin\Psi, \cos\Psi]^{\mathrm{T}}$, and the band normal in the reference configuration $\mathbf{n}_0$ is accordingly linked to the initial value of the band angle Ψ_0. In an updated reference frame, where the deformation gradient instantaneously coincides with the unit tensor ($\mathbf{F} = \mathbf{1}$) and the rate of the deformation gradient corresponds to the velocity gradient ($\dot{\mathbf{F}} = \mathbf{L}$), the traction continuity and compatibility conditions are expressed by the two tensor equations (Rice, 1976; Mear and Hutchinson, 1985; Needleman and Rice, 1978; Yamamoto, 1978; Morin et al., 2018)

$$\mathbf{n} \cdot \dot{\mathbf{P}}^{\mathrm{b}} = \mathbf{n} \cdot \dot{\mathbf{P}} \tag{6a}$$

$$\mathbf{L}^{\mathrm{b}} = \mathbf{L} + \dot{\mathbf{q}} \otimes \mathbf{n} \tag{6b}$$

where superscript "b" refers to band quantities. The nominal stress tensor and velocity gradient are denoted by $\mathbf{P}$ and $\mathbf{L}$, respectively, while $\dot{\mathbf{q}}$ represents a non-uniformity of the velocity gradient across the imperfection band. Eqs. (6a) and (6b) imply that the mechanical quantities inside and outside the band evolve differently, which is a key characteristic of the imperfection band analysis. The difference between the velocity gradient inside the band $\mathbf{L}^{\mathrm{b}}$ and outside the band $\mathbf{L}$ is given by the velocity gradient jump $\boldsymbol{\Delta}\mathbf{L} = \dot{\mathbf{q}} \otimes \mathbf{n}$ and varies only in the $\hat{x}_2$-direction (Rudnicki and Rice, 1975; Rice, 1976).

The numerical analysis consists of calculating mechanical quantities for the outer blocks and transfer these quantities onto the band such that traction continuity and compatibility, i.e. Eqs. (6a) and (6b), are fulfilled. To this end, we first calculate the stress (Σ_i) and strain (E_i) history in the outer blocks for a given loading condition (defined by T and L) using the material model outlined in Section 3.1. The strain components in the outer blocks are calculated from the stretch components (λ_i) according to $E_i = \ln(\lambda_i)$. Next, we calculate the evolution of the band angle (Ψ) from the strain history outside the band, viz.

$$\tan(\Psi) = \exp\left(E_2 - E_1\right) \tan\left(\Psi_0\right) \tag{7}$$

and subsequently the traction components,[2]

$$t_1 = -\Sigma_1 \sin\Psi = -\Sigma_{\mathrm{III}} \sin\Psi, \quad t_2 = \Sigma_2 \cos\Psi = \Sigma_{\mathrm{I}} \cos\Psi \tag{8}$$

from the band angle and stress quantities outside the band. The traction components t_i are imposed directly onto the top surface, while the displacement components u_1 and u_2 on the top surface are constrained to vary linearly with the $\hat{x}_1$-coordinate.[3] PBCs are assigned between the right and left surfaces to permit localization in the band direction and compatibility is enforced by specifying the relative displacement between corresponding nodes on the right and left surfaces according to

$$u_1^{\mathrm{right}} - u_1^{\mathrm{left}} = 2L_1\left(\exp(E_1) - 1\right) \tag{9a}$$

$$u_2^{\mathrm{right}} - u_2^{\mathrm{left}} = 2L_1\left(\exp(E_1)\tan\Psi - \tan\Psi_0\right) \tag{9b}$$

The symmetry condition, in addition to Eq. (6b), implies that the displacement components on the surfaces with normal in x_3-direction are given by

$$u_3^{\mathrm{back}} = -L_3\left(\exp(E_3) - 1\right) \tag{10a}$$

$$u_3^{\mathrm{front}} = 0 \tag{10b}$$

where "back" refers to the external surface and "front" refers to the mid-section cutting through the void, both having a unit normal in the x_3-direction.

Following the notation of Tekoğlu et al. (2015), the displacements and displacement rates in the region above and below the imperfection band are written

$$u_i = \left(\lambda_i - 1\right) X_i \pm \Delta_i \quad \Leftrightarrow \quad \dot{u}_i = \dot{\lambda}_i X_i \pm \dot{\Delta}_i \tag{11}$$

[2] Note that the traction components depicted in Fig. 5, $\hat{t}_i$, are given in the local coordinate system.

[3] The top and bottom surfaces of the band are expected to slightly perturb by the periodic array of voids within the band, which is neglected here; see also Tekoğlu et al. (2015).

where X_i are the reference coordinates, $(\lambda_i - 1)X_i$ represents the continuation of the uniform deformation across the band region, and Δ_i are additional rigid displacements of the outer blocks due to the imperfection. The additional displacements and their rates $(\Delta_i, \dot{\Delta}_i)$ are expressed in the global coordinate system. The values for $\dot{\Delta}_1$ and $\dot{\Delta}_2$ are generally non-zero, while it follows from compatibility requirements that $\dot{\Delta}_3 \equiv 0$. Then, the non-uniformity across the band can be written

$$\dot{q}_i = \frac{2\dot{\Delta}_i}{\bar{l}} \tag{12}$$

where $\bar{l}$ corresponds to the current thickness of the band, i.e. the height of the unit cell in the direction of $\hat{x}_2$ (see Fig. 5) in the deformed configuration. Using the compatibility condition Eq. (6b), the components of the velocity gradient jump in the global system, $\Delta L_{ij} = \dot{q}_i n_j$, are given by

$$\Delta L_{11} = -\frac{2\dot{\Delta}_1 \sin\Psi}{\bar{l}},\ \Delta L_{22} = \frac{2\dot{\Delta}_2 \cos\Psi}{\bar{l}},\ \Delta L_{12} = \frac{2\dot{\Delta}_1 \cos\Psi}{\bar{l}},\ \Delta L_{21} = -\frac{2\dot{\Delta}_2 \sin\Psi}{\bar{l}} \tag{13}$$

which then yield expressions for the rate-of-deformation components inside the band, viz.

$$D^{\mathrm{b}}_{11} = \dot{E}_1 - \frac{\dot{\Delta}_1 \tan(\psi)}{l_2} \tag{14a}$$

$$D^{\mathrm{b}}_{22} = \dot{E}_2 + \frac{\dot{\Delta}_2}{l_2} \tag{14b}$$

$$2D^{\mathrm{b}}_{12} = \frac{\dot{\Delta}_1 - \dot{\Delta}_2 \tan(\psi)}{l_2} \tag{14c}$$

where $\dot{E}_i$ refer to the strain rate components outside the band and l_i denote the unit cell dimensions in the deformed configuration expressed in the global (non-rotating) coordinate system. The shear components D^{b}_{12} inside the band are only governed by the additional displacement rates $\dot{\Delta}_i$, since there is no shear strain in the outer blocks. We note that the expressions given in Equation (2.11) in Tekoğlu et al. (2015) are retrieved if Eqs. (14a)–(14c) are transformed to the local coordinate system $\hat{x}_i$.

Macroscopic localization coincides with the instance when the analysis terminates due to a diverging solution. Prior to the onset of macroscopic localization, the increments of Δ_1 and Δ_2 follow from the prescribed stresses and strains in the outer blocks and the requirements of equilibrium and compatibility (see Eqs. (6a) and (6b)). Beyond the onset of macroscopic localization, the deformation of the band is not unique in that it depends on the unknown constraints of the outer blocks. Following the approach of Tekoğlu et al. (2015), the simulations are continued beyond macroscopic localization by prescribing the displacement increments of the band in a proportional manner governed by the ratio $\dot{\Delta}_1/\dot{\Delta}_2$ calculated from the last increment prior to the onset of macroscopic localization.

For every macroscopic stress state (T and L), we impose a range of initial band orientations Ψ_0 and search for the orientation that gives the lowest strain at localization with a precision corresponding to $\Delta\Psi_0 = 1°$. The orientation that gives the lowest strain at localization is referred to as the critical orientation. Since the numerical simulations are associated with finite increments, the predictions for macroscopic localization are slightly conservative but this difference is considered negligible in the current context. For further details regarding the FE band model, the reader is advised to consult the article by Tekoğlu et al. (2015).

4. Results and discussion

The equivalent stress and strain quantities referred to in the following are calculated from the volume-average stress and strain components according to

$$\Sigma_{\mathrm{eq}} = \sqrt{\frac{3}{2}\Sigma'_{ij}\Sigma'_{ij}}, \quad E_{\mathrm{eq}} = \int_0^t \sqrt{\frac{2}{3}D_{ij}D_{ij}}\,\mathrm{d}\bar{t} \tag{15}$$

where Σ'_{ij} are components of the deviatoric Cauchy stress tensor and D_{ij} are the components of the rate of deformation (Eulerian strain rate) tensor. Note that the equivalent stress and strain measures are not work conjugate and are only used to present the results. In the data corresponding to Models B and C, we make use of superscript "b" to label quantities that are calculated from inside the band. These are referred to as band quantities. Unless otherwise stated, quantities without a superscript correspond to volume averages over the entire material body associated with each model. These are referred to as macroscopic quantities. In the case of Model A, there is no distinction between macroscopic and band quantities. In the case of Model C, calculating the volume average over the entire model corresponds to calculating the quantities belonging to the outer blocks, due to the *a priori* assumption of infinite extension. All results presented for Models B and C pertain to the critical orientation of the unit cell, i.e. the initial orientation that yields the lowest strain at localization, as defined in the last paragraphs of Sections 3.4 and 3.5.

4.1. Mechanical behaviour

Figs. 6 and 7 present the evolution of the equivalent stress (top row) and the void volume fraction (bottom row) as a function of the equivalent strain for the three models. Fig. 6 corresponds to varying stress triaxiality T for a generalized tension loading $L = -1$, whereas Fig. 7 corresponds to varying Lode parameter L for a stress triaxiality $T = 0.75$. For Models B and C, the curves indicated with solid lines correspond to macroscopic quantities, whereas dashed lines refer to band quantities. Only a single, solid

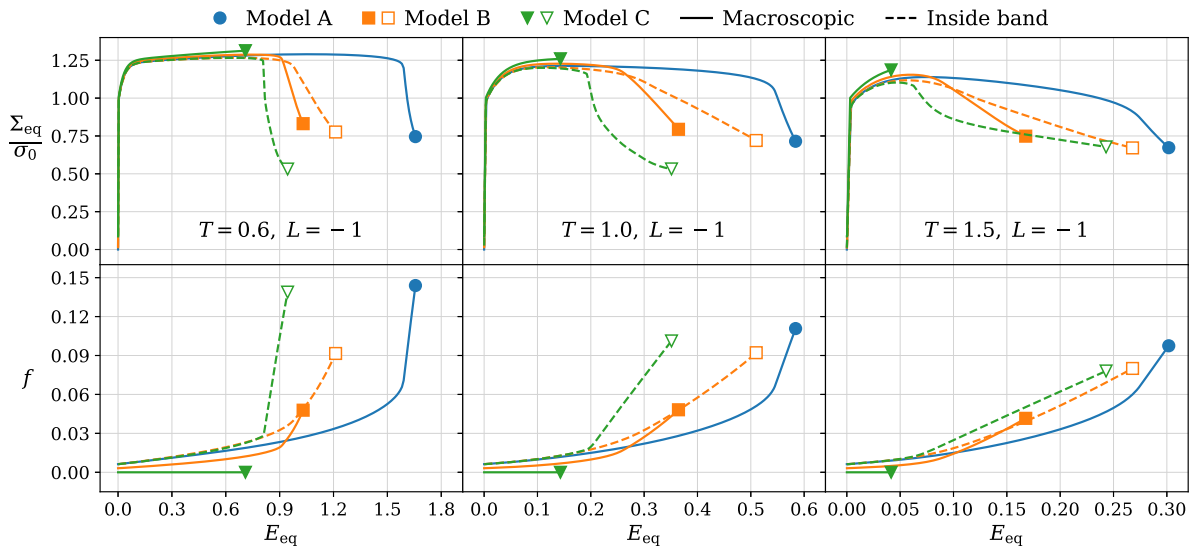

Fig. 6. Normalized stress–strain and void volume fraction data for all three models at different stress triaxiality ratios and a Lode parameter of $L = -1$.

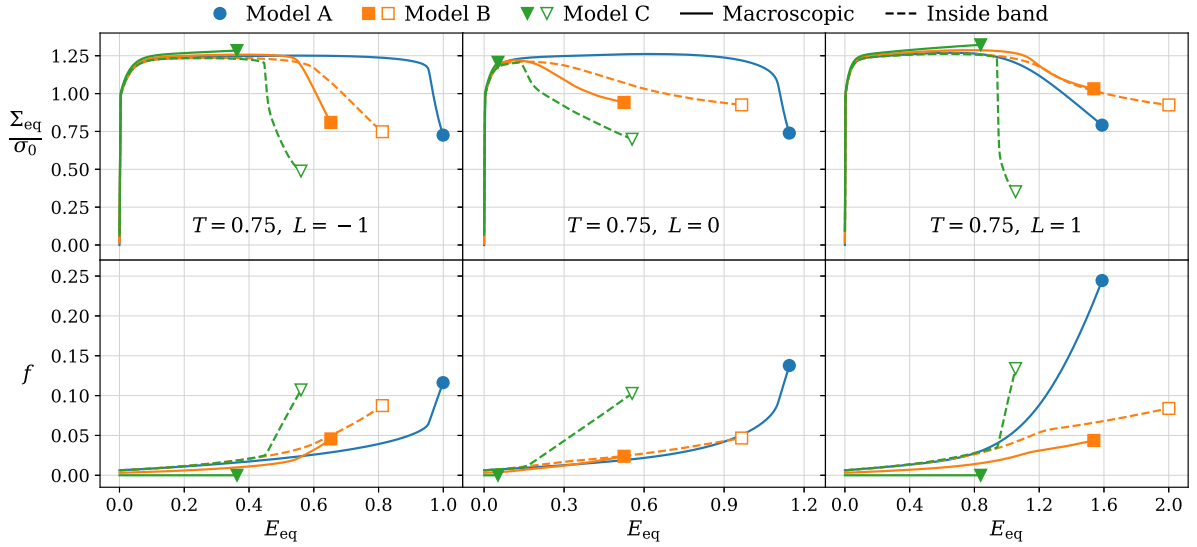

Fig. 7. Normalized stress–strain and void volume fraction data for all three models at different values of the Lode parameter and a stress triaxiality ratio of $T = 0.75$.

line is drawn for Model A, since quantities within the band coincide with the macroscopic ones. The macroscopic stress is not plotted beyond the onset of macroscopic localization for Model C.

We readily see from Figs. 6 and 7 that all models share some common features. The stress–strain curves display a peak stress, which separates the material response into a stable hardening phase and a softening phase. The softening phase introduces a possibility for a mechanical instability (Rice, 1976) that causes a rapid loss of load-carrying capacity and an associated rapid increase of the void volume fraction.

Besides certain commonalities, the three models display important differences, rooted in the assumptions governing each model. For Models B and C, the band quantities in Figs. 6 and 7 are seen to clearly differ from their macroscopic counterparts. While the void volume fraction and equivalent strain are larger in the band, the equivalent stress is larger in the outer blocks. This causes a different slope of the stress–strain curve inside the band compared to the macroscopic stress–strain curve, which is most pronounced in the softening phase. The difference between macroscopic quantities and band quantities increases with increasing stress triaxiality ratio, as inferred from Fig. 6. This tendency is also implied in the work of Tekoğlu et al. (2015), where they report that the instance of macroscopic localization coincides with the onset of void coalescence for lower values of stress triaxiality ($T \lessapprox 1$ in their work) and becomes increasingly different with increasing stress triaxiality. Since the material inside the band can yield by volumetric

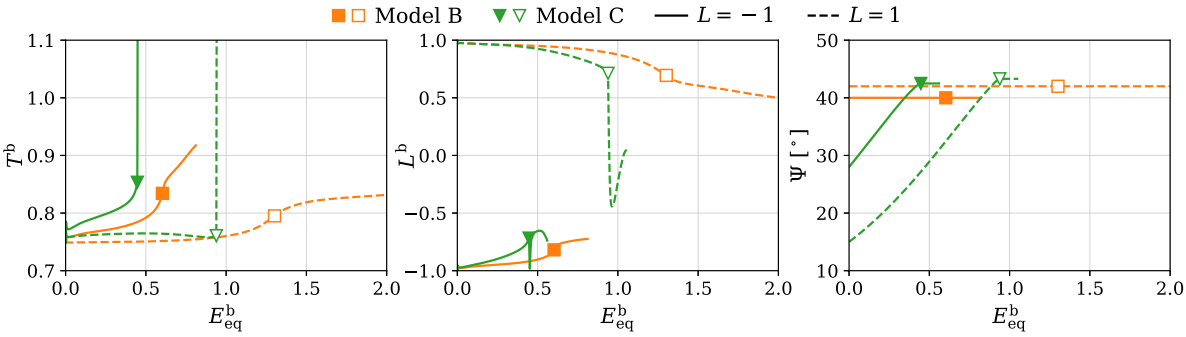

Fig. 8. Evolution of quantities inside the band with respect to the equivalent strain: stress triaxiality T^b (left), Lode parameter L^b (middle), and band angle Ψ (right). The markers plotted on the graphs indicate the point of macroscopic strain localization.

deformation, whereas the outer blocks cannot, the effect of the porosity inside the band becomes more visible when the hydrostatic stress component increases. As the stress triaxiality increases, the material outside the band undergoes less plastic deformation while the material inside the band continues to yield by volumetric plastic straining. This increases the mismatch between the field quantities inside and outside the band. If the macroscopic stress triaxiality ratio is sufficiently high, the band material would yield by plastic deformation while the outer blocks are still in the elastic domain. This suggests that the material displays a quasi-brittle failure mode for high stress triaxiality ratios, as previously discussed by Morin et al. (2018).

Although the band has a finite porosity that evolves with the macroscopic deformation, the macroscopic void volume fraction in Model C is zero because the two outer blocks are semi-infinite (or, conversely, the imperfection band is infinitely thin), as indicated in Figs. 6 and 7. Model C thus represents an abrupt and strong material imperfection in the otherwise homogeneous and non-porous solid that gives rise to a larger difference between the quantities inside and outside the imperfection band. This is indicated by the rapid evolution of the stress triaxiality ratio (T^b) and the Lode parameter (L^b) within the band in the case of Model C, as shown in Fig. 8. Conversely, Model B exhibits a slower evolution of the quantities inside the band, since the finite extension of the unit cell model in that case represents a weaker material imperfection.

In the case of Model C, the transition from the pre-localization step to the post-localization step is associated with an apparent jump in the band quantities. When the onset of macroscopic localization is reached, the analyses are continued by prescribing the deformation increments of the band, as explained in Section 3.5. This causes a jump in the stress state that is readily confirmed from the evolution of T^b and L^b shown in Fig. 8. The transition from the pre-localization step to the post-localization step is highlighted by markers ($\triangledown, \square$) on the graphs. Model B displays a more gradual transition because the unit cell is finite-sized and is subjected to the same macroscopic boundary conditions throughout the simulation.

An important difference between Models B and C, apart from the finite-sized outer blocks in the former, is that the spatial orientation of the imperfection band (Ψ) is kept fixed in Model B, as shown in the rightmost plot in Fig. 8. The imperfection band in Model C, on the other hand, rotates with the macroscopic deformation, and only becomes fixed in the post-localization stage. Interestingly, the critical band orientation angles for Models B and C are rather close, although the initial angle (Ψ_0) for Model C is very different, as seen from Fig. 8.

4.2. Influence of failure criterion

Micromechanically-based computational models are frequently used to predict ductility associated with material instability. However, establishing a rigorous criterion that provides precise predictions for various models at the microstructural level has proven difficult, which is reflected by the diversity in the failure criteria previously proposed and used in the literature. This difficulty is highlighted in a study by Dæhli et al. (2017b), where the authors have shown that the predicted failure loci change both shape and magnitude depending upon the criterion used to evaluate failure initiation in the numerical analyses. Also, the work of Luo and Gao (2018) discusses the influence of the adopted failure criterion in unit cell studies. This section compiles some of the criteria that are found in the literature and demonstrates how the mechanical quantities associated with each criterion evolve during the simulations and affect the failure predictions.

The onset of material softening, i.e. $\mathrm{d}\Sigma_{eq} = 0$, is a possible definition of ductile failure that has been widely used in unit cell studies (see e.g. Dahl et al. (2012), Nielsen et al. (2012), Tvergaard (2012), Bomarito and Warner (2015, 2017) and Xiao et al. (2021)). This criterion is generally rather conservative and corresponds to the earliest possible point of material instability for an isotropic solid obeying the associated flow rule (Rice, 1976; Needleman and Rice, 1978). However, the graphs in Figs. 6 and 7 show that for Model C, and also for Model B if $L_2 \gg L_1$, the heterogeneity embodied in the framework of the imperfection band analyses permits localization to occur for positive macroscopic hardening values. Thus, in the case of Model C, we have used the peak value of the average stress within the band region rather than the macroscopic value.[4]

[4] The predictions using macroscopic peak stress would coincide with macroscopic localization – which is accounted for by another failure indicator presented below – and is thus redundant.

Perhaps the most widely used criterion, stemming from the work of Koplik and Needleman (1988), is to associate failure by void coalescence with the instance when the macroscopic deformation shifts to a uniaxial straining mode (see e.g. Søvik and Thaulow (1997), Kim et al. (2004), Gao and Kim (2006), Gao et al. (2010), Steglich et al. (2010), Zhang and Skallerud (2010), Keralavarma et al. (2011), Benzerga et al. (2012), Tekoğlu (2014), Dæhli et al. (2016), Morin et al. (2019), Frodal et al. (2019) and Dæhli et al. (2020)). In the case of computational models similar to Model A, the shift to uniaxial straining corresponds to plastic flow localization in the intervoid ligaments, which is usually followed by a rapid drop in the macroscopic stress and accelerated void growth, as observed in Figs. 6 and 7. This facilitates void coalescence by internal necking. However, a shift to uniaxial straining mode never occurs for some stress states (i.e. for some T and L combinations, see also Tekoğlu (2014)). Therefore, despite its clear physical interpretation, this criterion cannot be used for all loading conditions.

Failure in band-type models, such as Models B and C, can be associated with a rapid increase of some measure of the deformation rate inside the band compared to that in the outer blocks (Needleman and Tvergaard, 1992). Such a definition of failure has been used in many numerical studies based on micromechanical modelling of ductile fracture (see e.g. Barsoum and Faleskog (2007, 2011), Dunand and Mohr (2014), Tvergaard (2015) and Dæhli et al. (2017b)). To this end, we define the ratio between the equivalent strain rate inside and outside the band, viz.

$$\xi_{\mathrm{D}} = \frac{\dot{E}^{\mathrm{b}}_{\mathrm{eq}}}{\dot{E}^{\mathrm{o}}_{\mathrm{eq}}} \approx \frac{\Delta E^{\mathrm{b}}_{\mathrm{eq}}}{\Delta E^{\mathrm{o}}_{\mathrm{eq}}} \tag{16}$$

where $\dot{E}_{\mathrm{eq}} = \sqrt{2/3 D_{ij} D_{ij}}$ is the equivalent strain rate. Note that the distinction between $\Delta E^{\mathrm{o}}_{\mathrm{eq}}$ and ΔE_{eq}, i.e. *outside* and *macroscopic*, is only relevant for Model B, since the region outside the band is of finite size. Strain localization in the band is then, in theory, associated with the instance when $\xi_{\mathrm{D}} \to \infty$, but we assume that the asymptotic value is reached at a threshold value of $\xi_{\mathrm{D}} = 50$. A similar criterion has been adopted in the unit cell study by Luo and Gao (2018), but in that case failure was defined as the instance when the strain in the two outer layers reaches a constant level. For any practical purpose, this corresponds to ξ_{D} reaching a large value.

Wong and Guo (2015) and Liu et al. (2016) proposed to define failure in unit cell analyses from energy considerations. Following their approach, we define the ratio between the rate of strain energy $\dot{W}_{\mathrm{e}}$ and the plastic dissipation $\dot{W}_{\mathrm{p}}$, viz.

$$\xi_{\mathrm{W}} = \frac{\dot{W}_{\mathrm{e}}}{\dot{W}_{\mathrm{p}}} \approx \frac{\Delta W_{\mathrm{e}}}{\Delta W_{\mathrm{p}}} \tag{17}$$

As stated by Liu et al. (2016), the ratio ξ_{W} gives three distinct states:

(1) $\xi_{\mathrm{W}} > 0$ indicates elastic loading,
(2) $\xi_{\mathrm{W}} = 0$ indicates neutral loading,
(3) $\xi_{\mathrm{W}} < 0$ indicates elastic unloading.

Failure could potentially take place as long as $\xi_{\mathrm{W}} < 0$, and the strain level when $\xi_{\mathrm{W}} = 0$ for the first time is then judged as a conservative estimate of the fracture strain. Note that for Model C, the strain energy and plastic work is calculated over the band region, and not over the entire model, because the material outside the band continuously strain hardens until the onset of localization. That is, the ratio ξ_{W} would not become negative – and failure would not be detected – if it were to be calculated over the entire model. The results of Wong and Guo (2015) and Liu et al. (2016) show that the shift to a uniaxial straining mode coincides with the instance when ξ_{W} reaches a minimum, i.e. $\xi_{\mathrm{W}} = \xi_{\mathrm{W,min}}$. From a physical point-of-view, the rationale for this failure criterion is that void coalescence is associated with plastic flow localization in the intervoid ligament and a rapid release of strain energy.

Figs. 9 and 10 show graphs for the evolution of four different quantities that can be used to define failure. Fig. 9 pertains to generalized tension, i.e. $L = -1$, and various stress triaxiality ratios, whereas Fig. 10 pertains to varying values of the Lode parameter and a stress triaxiality ratio of $T = 0.75$. The first row in these figures corresponds to the normalized intermediate principal strain ($|E_{\mathrm{II}}|/\max(|E_{\mathrm{II}}|)$) and the point where uniaxial straining takes place is indicated by a square marker (□). The evolution of the strain rate ratio ξ_{D} is shown in the second row and the associated point of failure, taken to be $\xi_{\mathrm{D}} = 50$, is highlighted by a triangular marker (▽). This criterion cannot be evaluated for Model A due to the equivalence between the macroscopic and band quantities, and the ratio is consequently set to unity. In the third row, graphs pertaining to the ratio between elastic and plastic power (ξ_{W}) are shown and the points associated with incipient neutral loading (i.e. $\xi_{\mathrm{W}} = 0$) and the minimum value ($\xi_{\mathrm{W}} = \xi_{\mathrm{W,min}}$) are indicated by diamond (◇) and circle (○) markers, respectively. The last row shows the evolution of the ratio between the volume that undergoes plastic straining V_{p} and the total volume of the band region V_{tot}.[5] All the points associated with the four failure criteria are plotted on top of these graphs ($V_{\mathrm{p}}/V_{\mathrm{tot}}$) to facilitate a comparison. The equivalent strain is calculated from the band quantities in Model C and from the macroscopic quantities for Models A and B.

Tekoğlu et al. (2015) have shown that macroscopic localization and void coalescence are distinct phenomena that could occur simultaneously, depending upon the stress state. While both phenomena refer to the localization of deformation, they take place at different scales. *Macroscopic localization* corresponds to the shift from a homogeneous macroscopic deformation to a localized straining mode, where the continuing deformation primarily takes place within a zone whose size is set by the microstructural heterogeneity (see e.g. Tekoğlu and Nielsen (2019), Andersen et al. (2020) and Çelik et al. (2021)). This corresponds to the size

[5] This means the entire FE model for Models A and C, while it refers to the middle region of Model B, see Fig. 4.

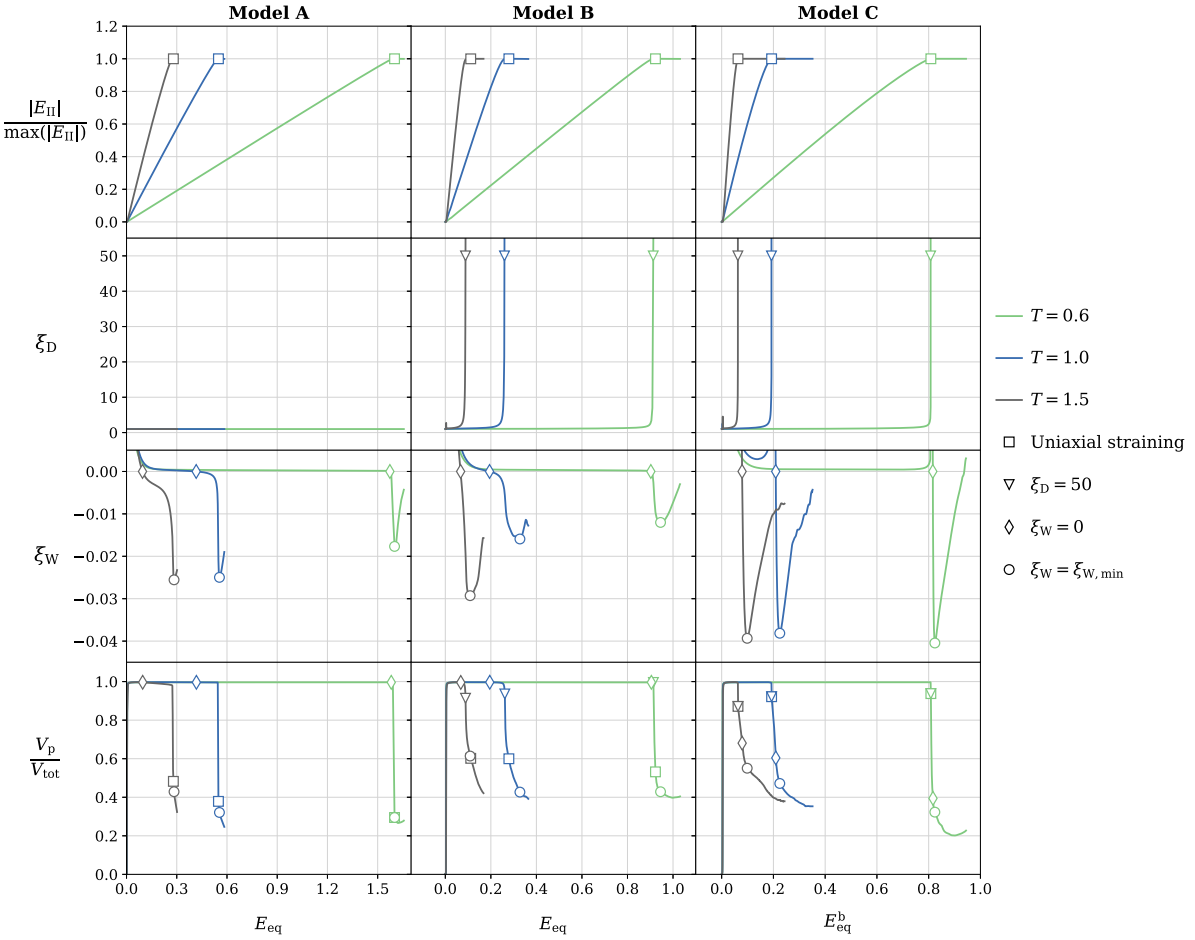

Fig. 9. Evolution of different failure indicator quantities, with the macroscopic equivalent strain for Models A and B, and with the equivalent strain in the band for Model C. The Lode parameter is set to $L = -1$ for all the curves, while the stress triaxiality ratio changes from $T = 0.6$ to 1.5.

of the entire unit cell in the current work, which is dictated by the void spacing in the periodic void array. Although macroscopic localization could occur in zones that span several voids,[6] the analyses herein are restricted to localization taking place across a single array of voids. *Void coalescence* corresponds to plastic flow localization emanating from neighbouring voids and progressing through the intervoid ligaments. Thus, void coalescence occurs due to strain localization within the unit cell in a zone that is smaller than the overall unit cell size and with a width set by the void size. Given the scope of this study, it is imperative to adopt the same failure criteria to each model to facilitate an unbiased comparison between them.

In Model C, onset of macroscopic localization follows naturally from the analyses when the continuing equilibrium and compatibility conditions can no longer be satisfied. This corresponds to $\xi_D \to \infty$, as seen from Figs. 9 and 10. Similar conditions pertain to Model B, where a rapid increase of ξ_D suddenly takes place. In Model A, however, there is no such point and incipient macroscopic localization cannot be evaluated. In a material comprising a uniform void distribution, such as Model A, it might be argued that macroscopic localization coincides with onset of void coalescence. However, this argument cannot be extended to general cases since material heterogeneities that give rise to macroscopic strain localization invariably exist in real materials. Two possible definitions of macroscopic strain localization for Model A could be either the peak stress or the point where $\xi_W = 0$. Since neither of these generally conform with the criterion governing Models B and C, they will not be adopted herein. The only viable alternative would be to establish the material tangent stiffness for the unit cell in Model A at each increment of the analysis, and evaluate the determinant of the acoustic tensor such that $\det(\mathbf{n} \cdot \mathbf{C}^t \cdot \mathbf{n}) = 0$ (e.g. Zhu et al., 2020a,b), but this method is not pursued herein.

Onset of void coalescence in unit cell simulations is traditionally associated with the shift to a macroscopic uniaxial straining mode following the work of Koplik and Needleman (1988). It is however not certain that this criterion applies to all the different models studied here, as implied by the results shown in Figs. 9 and 10. Consider the graphs in the bottom row, which show the

[6] This could be included by modelling several voids across the height of the band.

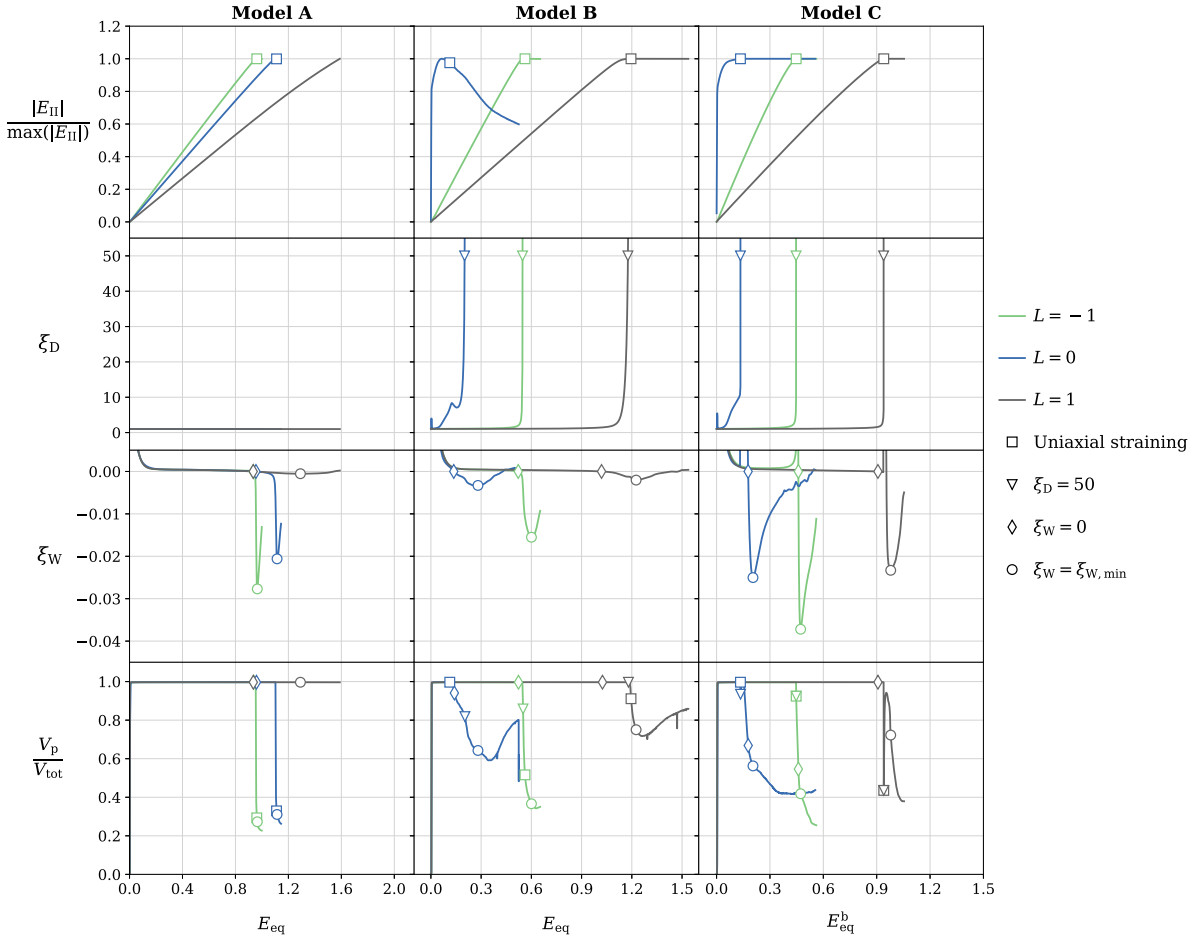

Fig. 10. Evolution of different failure indicator quantities, with the macroscopic equivalent strain for Models A and B, and with the equivalent strain in the band for Model C. The stress triaxiality ratio is set to $T = 0.75$ for all the curves, while the Lode parameter changes from $L = -1$ to 1.

evolution of the ratio V_p/V_{tot} with the equivalent strain. The failure points associated with the various failure criteria are plotted on top of each curve to aid the interpretation and assessment of their impact on the resulting predictions. In the case of Model A, we find a general conformity between the onset of uniaxial straining (□) and the point where $\xi_W = \xi_{W,min}$ (○), corroborating the results in Liu et al. (2016). When $L = 1$, a state of uniaxial straining is not attained, which makes it impossible to use uniaxial straining as a void coalescence criterion for Model A. For Model B, uniaxial straining (□) usually takes place somewhere between the points where $\xi_D = 50$ (▽) and $\xi_W = \xi_{W,min}$ (○), with an exception pertaining to $L = 0$. The slight variation could be a numerical effect due to the finite threshold value chosen to indicate uniaxial straining, but it seems natural that uniaxial straining becomes coincident with macroscopic localization when the unit cell is relatively high (i.e. $L_2 \gg L_1$). This is substantiated by the results for Model C, where the onset of uniaxial straining coincides with the point where $\xi_D \to \infty$ since the deformations outside the band cease when macroscopic localization initiates. The criterion based on uniaxial straining thus has different physical interpretation depending upon the unit cell model. In the case of Model C, using uniaxial straining as a coalescence criterion is synonymous to stating *a priori* that macroscopic localization and void coalescence occur simultaneously. Since void coalescence is associated with localization of plastic flow within the unit cell, the number of integration points that have a non-zero plastic strain rate $\dot{p} > 0$, i.e. the volume that undergoes plastic straining V_p, should reach a nearly constant value during void coalescence. From the lower row of graphs in Figs. 9 and 10, we observe that $\xi_W = \xi_{W,min}$ is typically reached when V_p tends to saturate. It transpires that $\xi_W = \xi_{W,min}$ is a more promising void coalescence criterion.

To summarize, in this study:

- macroscopic localization is defined by $\xi_D = 50$ in Model B, and is associated with the termination of the first loading step in Model C,
- void coalescence is defined by $\xi_W = \xi_{W,min}$.

In the sequel, we also present results pertaining to the point of peak stress, since this criterion is widely used and generally gives rather different results than the other two.

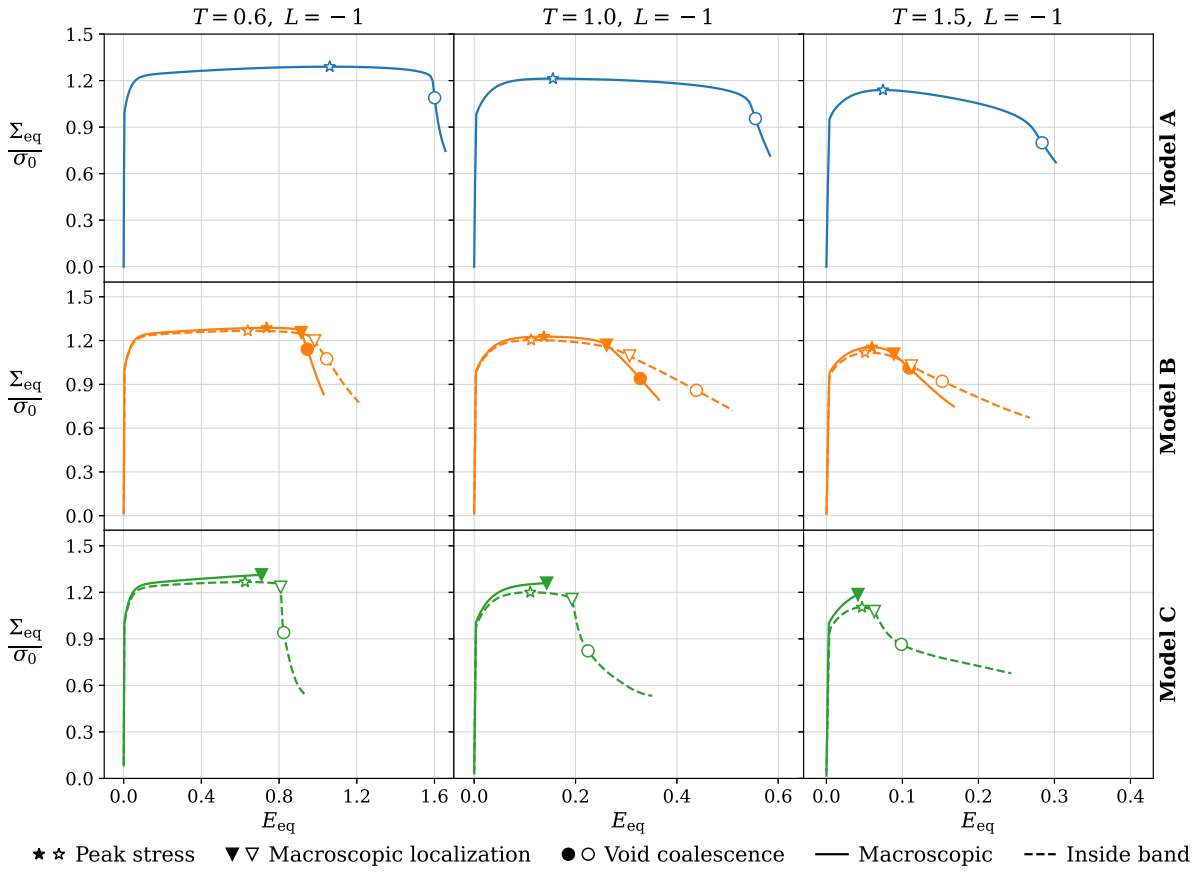

Fig. 11. Macroscopic equivalent stress–strain curves for the various models at different values of the stress triaxiality ratio in generalized tension ($L = -1$). Points for peak stress (☆), macroscopic localization (▽), and void coalescence (○) are indicated on the graphs. The results correspond to Model A (top row), Model B (middle row), and Model C (bottom row).

4.3. Distinction between peak stress, macroscopic localization and void coalescence

Macroscopic equivalent stress–equivalent strain curves are plotted in Fig. 11 for $L = -1$ and varying T, and in Fig. 12 for $T = 0.75$ and varying L. Data pertaining to Model A are shown in the top row, Model B in the middle row, and Model C in the bottom row. The points where peak stress (☆), macroscopic localization (▽), and void coalescence (○) take place are highlighted on each graph. Solid lines and filled markers are used for the macroscopic quantities, while dashed lines and open markers are used for band quantities. Note that there is no point associated with macroscopic localization for Model A, since it cannot be determined with the criterion adopted here. For Model C, the macroscopic response is only plotted up the onset of macroscopic localization.

The graphs show that peak stress, macroscopic localization, and onset of void coalescence are generally distinct points based on the current failure criteria. In general, the strain at peak stress is a conservative estimate for the ductility. However, the difference between the strain at peak stress, macroscopic localization, and void coalescence depends upon the stress state, the model employed, and whether macroscopic or band quantities are considered. In Model A, the difference between the strains at peak stress and at void coalescence is very large, but diminishes with decreasing stress triaxiality. In Models B and C, the failure strain predicted from the various failure criteria depends upon whether we consider the macroscopic quantities or the band quantities. The difference between the strains at peak stress, macroscopic localization, and void coalescence is smaller in terms of macroscopic quantities than in terms of band quantities. Except for loading cases with a high stress triaxiality or with $L = 0$ using Model C, the peak stress inside the band is reached sooner than the macroscopic peak stress due to the void-induced softening. For Model C, the macroscopic strains at peak stress, macroscopic localization, and void coalescence coincide.

The distinction between macroscopic localization and void coalescence was clearly presented by Tekoğlu et al. (2015). In their work, void coalescence was defined as the instance when the ratio between the maximum and minimum plastic strain rate at the void surface first exceeded a value of 15. This criterion clearly reflects key characteristics of the void coalescence process, but is susceptible to local differences in the spatial field quantities and the mesh size in the void region. In the current study, onset of void coalescence is defined by $\xi_W = \xi_{W,min}$ (cf. Section 4.2), which is based on average properties from inside the band and is less affected by mesh size. Note that this criterion still reflects the local concentration of plastic straining within the band. Despite

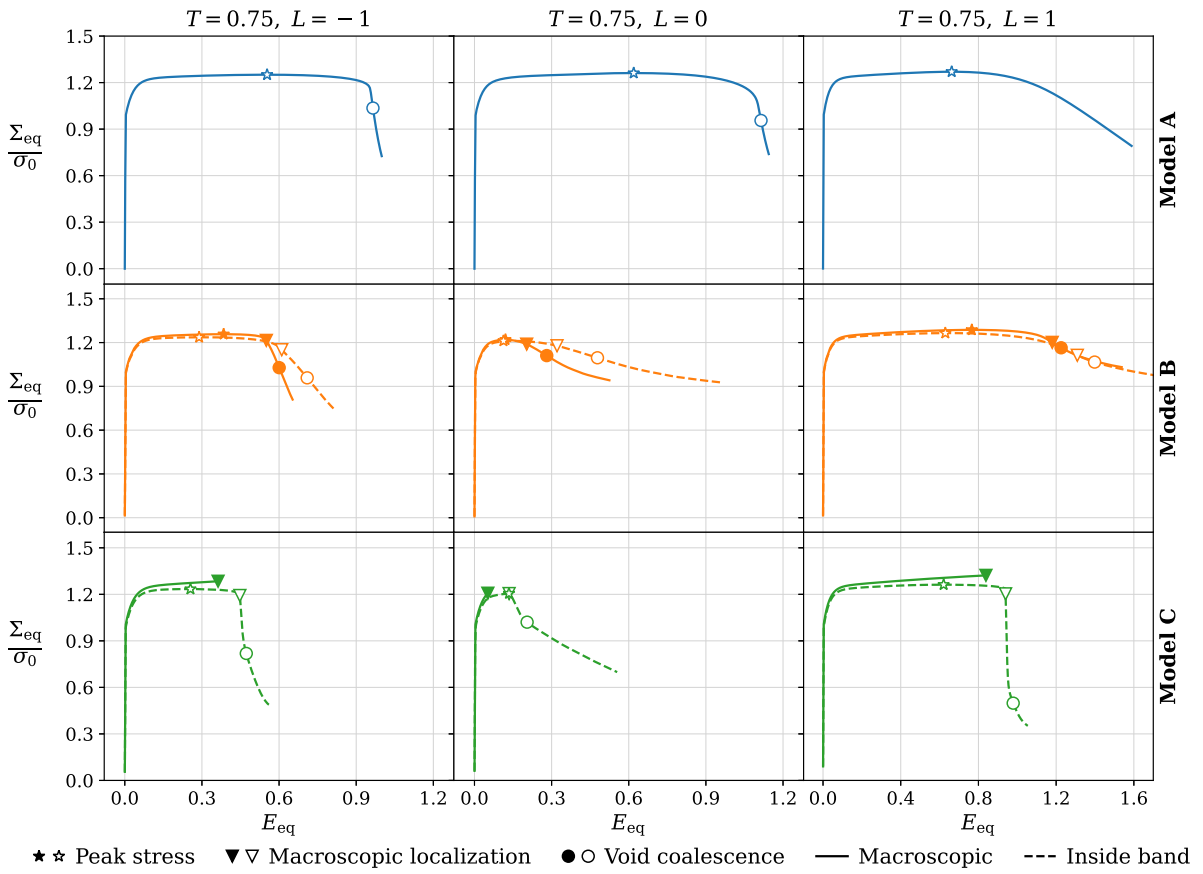

Fig. 12. Macroscopic equivalent stress–strain curves for the various models at three different values of the Lode parameter ($L = -1,\ 0,\ 1$) when $T = 0.75$. Points for peak stress (☆), macroscopic localization (▽), and void coalescence (○) are indicated on the graphs. The results correspond to Model A (top row), Model B (middle row), and Model C (bottom row).

the use of a different coalescence criterion, the results of Model C are in agreement with the results reported by Tekoğlu et al. (2015). In terms of band quantities, the onset of macroscopic localization and void coalescence are distinct, but coincide when the stress triaxiality is reduced. A somewhat conflicting result was reported by Guo and Wong (2018), where the onset of macroscopic localization and void coalescence was found to coincide for high values of stress triaxiality. They employed a unit cell similar to Model B, but used a different criterion for the onset of macroscopic localization, which is rather similar to the criterion $\xi_W = 0$ discussed in Section 4.2. Since the same trend is not found for Model B in the current study, this demonstrates that the choice of failure criterion has significant influence on the results.

It should be noted that the observations from the numerical simulations are also influenced by whether we consider macroscopic quantities or band quantities. From a practical viewpoint, the macroscopic quantities are probably most important, since they are probed in experiments and structural assessments. However, more local measurements would be needed to evaluate and model the material behaviour beyond macroscopic localization. Based on the results of Model C, one would conclude that macroscopic localization and void coalescence are always simultaneous if the macroscopic quantities were considered. On the contrary, the finite size of the unit cell in Model B causes a more gradual transition from macroscopic localization to void coalescence, and macroscopic localization and void coalescence are thus always distinct. Note that Model B facilitates a variety of gauge sizes – either by changing the height of the unit cell or by volume-averaging quantities over sub-regions in the model – and would become quite similar to Model C if $L_2 \gg L_1$. It follows that a clear distinction between macroscopic localization and void coalescence, as reported in previous studies (e.g. Tekoğlu et al. (2015) and Guo and Wong (2018)), depends on the resolution of the measured quantities. In reality, structural components and test specimens have finite dimensions and weaker initial imperfections than assumed in Models B and C, which would relax the difference between the outer blocks and the band. In turn, the results would be qualitatively more similar to Model B, and the distinction between macroscopic localization and void coalescence then follows accordingly.

4.4. Failure loci

Figs. 13–15 plot the failure strain at peak stress (left), at macroscopic localization (middle), and at the onset of void coalescence (right) with respect to the macroscopic stress state. Graphs indicated by blue lines with circle markers (○) correspond to Model A,

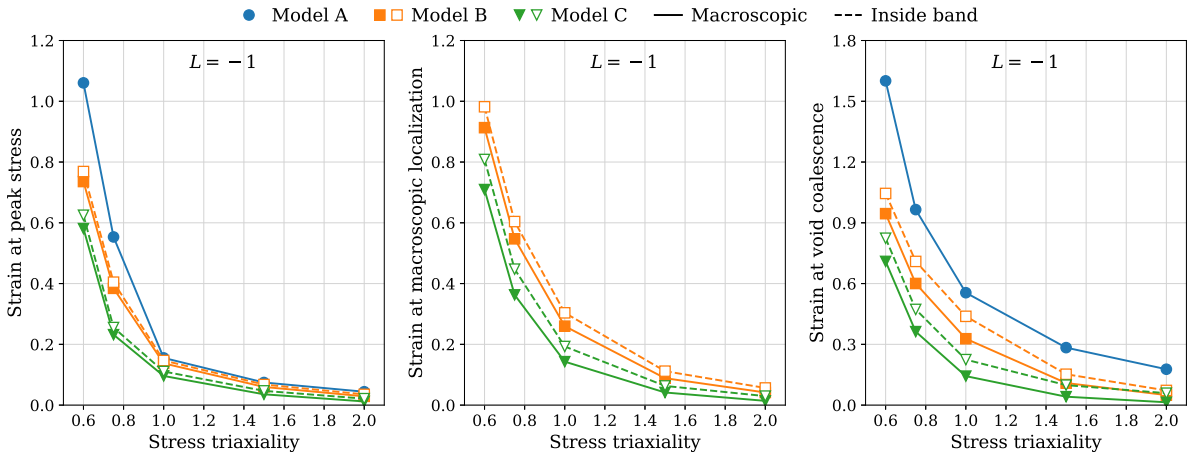

Fig. 13. Failure loci as a function of the stress triaxiality ratio T for a Lode parameter of $L = -1$.

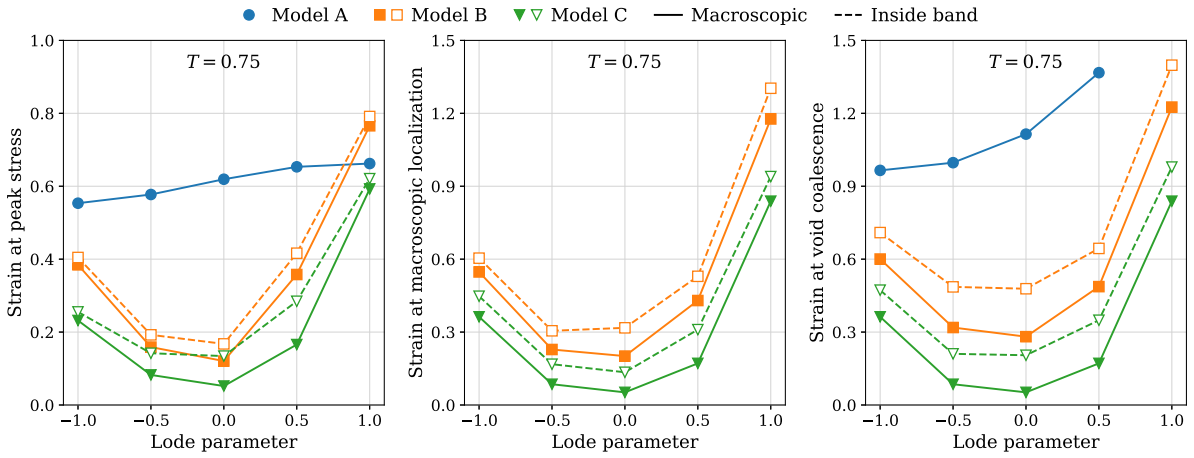

Fig. 14. Failure loci as a function of the Lode parameter L for a stress triaxiality ratio of $T = 0.75$.

orange lines with square markers (□) correspond to Model B, and green lines with triangular markers (▽) correspond to Model C. The macroscopic and the band quantities are plotted using solid and dashed lines, respectively. To highlight the effect of the stress state on the failure predictions, the failure loci are plotted either as a function of T while keeping the Lode parameter constant at $L = -1$ (Fig. 13) or as a function of L with constant stress triaxiality ratios $T = 0.75$ (Fig. 14) and $T = 2.0$ (Fig. 15).

The failure loci predicted from all three models appear rather similar in shape and display an exponential decrease of the failure strain with respect to the macroscopic stress triaxiality ratio (see Fig. 13) when the Lode parameter is kept constant. Note that we restrict the discussion to $L = -1$ here. The magnitude of the failure strain differs significantly between the models. Model C always gives the lower limit, whereas Model A usually gives the upper limit. The failure loci evaluated from band quantities are elevated compared to their macroscopic counterparts, which is reasonable due to the presence of the void. However, the shape of the failure loci are similar regardless of the quantities used for reference.

The qualitative conformity between the three models is interesting since it implies that these models can be used interchangeably, provided that the Lode parameter is fixed and that the failure locus is scaled to rule out the difference in magnitude seen from the graphs in Fig. 13. There are ductile failure models still used today that are not explicitly dependent on the Lode parameter (e.g. the ductile fracture criteria proposed by Cockroft and Latham (1968) and Johnson and Cook (1985)), or any other suitable measure of the deviatoric stress state. Such failure models could, at least in principle, be calibrated from either of the three models with limited influence on the numerical predictions since the shape of the failure locus would be similar. However, neither of the computational models should be used without at least one parameter being determined from material tests to scale the failure locus appropriately.

The three models display more pronounced differences when the stress triaxiality is kept constant and the Lode parameter is varied. The failure strain is highly dependent on the Lode parameter in all three models, as seen in Figs. 14 and 15, and the influence of the Lode parameter is greater when the stress triaxiality ratio is low (Barsoum and Faleskog, 2011; Dunand and Mohr, 2014; Luo and Gao, 2018). States of generalized tension ($L = -1$) always give a lower failure strain than states of generalized compression

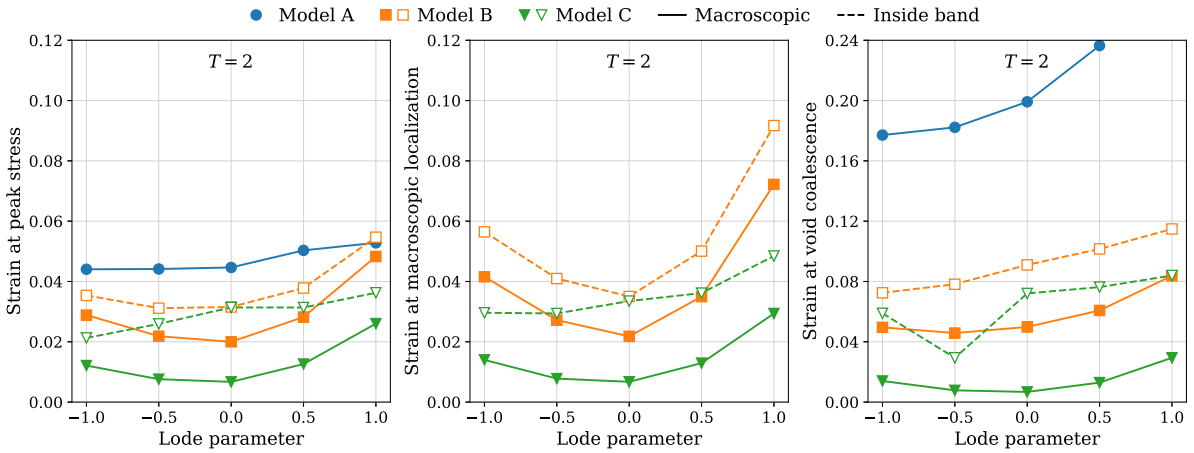

Fig. 15. Failure loci as a function of the Lode parameter L for a stress triaxiality ratio of $T = 2$.

($L = 1$), which conforms with previous studies in the literature (Gao and Kim, 2006; Barsoum and Faleskog, 2011; Wong and Guo, 2015; Tekoğlu et al., 2015; Vishwakarma and Keralavarma, 2019). In the case of Model A, the failure strain increases monotonically with the Lode parameter. This was also observed in other numerical studies (Gao and Kim, 2006; Yu et al., 2016; Dæhli et al., 2018) and was included in a heuristic extension of the Gurson model (Dæhli et al., 2018). In contrast, the failure loci of Models B and C are both non-monotonic and asymmetric with respect to the Lode parameter. This difference in shape between the failure loci of Model A and Models B and C is due to the preclusion of shear deformation in Model A. If a macroscopic shear stress is included in Model A, the results would become more similar to those of Model B.

In general, Models B and C exhibit a minimum failure strain for a stress state between generalized tension ($L = -1$) and generalized shear ($L = 0$). Lower stress triaxiality ratios typically lead to a minimum ductility close to generalized shear, whereas higher stress triaxiality ratios tend to drive the minimum ductility towards a state of generalized tension. Similar observations were reported by Dæhli et al. (2017b) and Morin et al. (2018). This effect manifests the underlying mode of localization: while a low stress triaxiality promotes localization by shearing between the upper and lower outer blocks surrounding the imperfection band, a high stress triaxiality promotes localization by an opening mode governed by extension of the imperfection band in the direction of the band normal. With reference to Eq. (12), if the components of the non-uniformity vector $\dot{q}_i$ were transformed to the local coordinate system (see $\hat{x}_i$ in Fig. 5 for reference), lower stress triaxiality ratios entail that $\dot{\hat{q}}_1$ is dominant, while higher stress triaxiality ratios entail that $\dot{\hat{q}}_2$ is dominant. This change of operative failure mode in Model C (from shear-type to extension-type) also has an interesting effect on the failure loci derived from the band quantities. As seen in Fig. 15, the failure locus inside the band displays a monotonic increase with respect to the Lode parameter, which is similar to the behaviour of Model A. Since the extension mode dominates over the shear mode when the stress triaxiality is high, the band is subjected to predominant normal loading, which is exactly what is imposed to Model A from the outset. A similar reasoning can explain the results pertaining to the onset of void coalescence in Model B at high stress triaxialities, as seen from the rightmost plot in Fig. 15.

The results elucidate that the influence of the Lode parameter on ductile failure depends on the boundary conditions used in the computational model. This dependency translates to ductile failure models intended for large-scale applications if micromechanical analyses are used to generate data for the calibration process or the development of new models. It transpires that the connection between micromechanically-based models and macroscopic models for ductile failure requires careful consideration in order to properly reflect the relevant failure mechanisms and give reliable predictions of the ductile failure strain. As a general remark, computational models similar to Model A might be appropriate in analyses of void growth or in conjunction with calibration of porous plasticity models without effects of shear deformation (e.g. the Gurson model), whereas Models B and C reflect the important mechanical phenomena of macroscopic localization and void coalescence and thus seem more appropriate for direct modelling of ductile failure.

5. Concluding remarks

We have examined the mechanical response and ductile failure predictions of three different micromechanically-based computational models for fracture in porous ductile solids. Model A is a unit cell model that represents a triply periodic distribution of spherical voids subjected to normal macroscopic loading, whereas Models B and C are finite-sized and semi-infinite finite element models of the imperfection band analysis (Rice, 1976). The models differ from the outset but are used somewhat interchangeably in the literature to study effects of microstructural features and loading conditions on ductile fracture. Numerical simulations have been performed for a range of macroscopic loading conditions. The main findings are summarized as follows:

- The applied computational model is decisive for the predicted mechanical response and the failure strain. Models B and C display non-monotonic and asymmetric failure loci with respect to the Lode parameter, whereas Model A exhibits a monotonic increase of the failure strain with the Lode parameter. This difference is rooted in the assumption of zero macroscopic shear stresses in Model A, which precludes shear localization and thus restricts the possible failure modes. However, the predicted failure loci of the three models are qualitatively similar when the stress triaxiality is varied while the Lode parameter is fixed.
- Various failure criteria to determine the onset of ductile failure have been expounded and shown to be of great significance for the failure strain predictions. This suggests that the failure criterion should be carefully chosen to obtain unambiguous results. Ultimately, we selected three different failure criteria that were used in the assessment:

  (i) peak stress ($\mathrm{d}\Sigma_{\mathrm{eq}} = 0$),
  (ii) macroscopic localization ($\xi_{\mathrm{D}} \to \infty$),
  (iii) void coalescence ($\xi_{\mathrm{W}} = \xi_{\mathrm{W,min}}$).

- The numerical simulations show that the strains at peak stress, macroscopic localization, and void coalescence are generally distinct. However, in the case of Model C, they coincide when the macroscopic quantities are considered.
- In Model B, and in Model C when the band quantities are considered, macroscopic localization usually takes place between the instance of peak stress and the onset of void coalescence, but may coincide with the former and/or the latter depending upon the stress state, the computational model, and the quantities used for reference. In Model C, the onset of macroscopic localization and void coalescence coincide when the stress triaxiality is intermediate, while macroscopic localization precedes void coalescence as the stress triaxiality increases. This finding corroborates the results of Tekoğlu et al. (2015).
- The predictions of Models B and C depend upon whether macroscopic quantities or band quantities are used in the assessment, and the failure strain is consistently larger when band quantities are considered.

In conclusion, this study shows that the three computational models give quite different results in terms of the evolution of mechanical quantities and the failure loci derived from the numerical analyses. As such, these models cannot be used interchangeably to examine effects of microstructural features and loading conditions on ductile failure. It further elucidates that micromechanical modelling and simulations should always be used cautiously in conjunction with calibration and development of ductile failure models used for large-scale simulations.

CRediT authorship contribution statement

Lars Edvard Blystad Dæhli: Conceptualization, Methodology, Validation, Formal analysis, Investigation, Visualization, Writing – original draft. **Cihan Tekoğlu:** Conceptualization, Methodology, Validation, Formal analysis, Investigation, Writing – review & editing. **David Morin:** Conceptualization, Methodology, Writing – review & editing. **Tore Børvik:** Conceptualization, Writing – review & editing, Supervision, Funding acquisition. **Odd Sture Hopperstad:** Conceptualization, Methodology, Writing – review & editing, Supervision, Project administration, Funding acquisition.

Declaration of competing interest

The authors declare that they have no known competing financial interests or personal relationships that could have appeared to influence the work reported in this paper.

Acknowledgements

The authors gratefully appreciate the financial support from NTNU and the Research Council of Norway through the FRIPRO programme, Project No. 250553 (FractAl).

References

Andersen, R.G., Tekoğlu, C., Nielsen, K.L., 2020. Cohesive traction–separation relations for tearing of ductile plates with randomly distributed void nucleation sites. Int. J. Fract. 224, 187–198. http://dx.doi.org/10.1007/s10704-020-00454-2.

Babout, L., Maire, E., Fougères, R., 2004. Damage initiation in model metallic materials: X-ray tomography and modelling. Acta Mater. 52 (8), 2475–2487. http://dx.doi.org/10.1016/j.actamat.2004.02.001.

Bao, Y., Wierzbicki, T., 2004. On fracture locus in the equivalent strain and stress triaxiality space. Int. J. Mech. Sci. 46, 81–98. http://dx.doi.org/10.1016/j.ijmecsci.2004.02.006.

Barsoum, I., Faleskog, J., 2007. Rupture mechanisms in combined tension and shear-Micromechanics. Int. J. Solids Struct. 44 (17), 5481–5498. http://dx.doi.org/10.1016/j.ijsolstr.2007.01.010.

Barsoum, I., Faleskog, J., 2011. Micromechanical analysis on the influence of the Lode parameter on void growth and coalescence. Int. J. Solids Struct. 48, 925–938. http://dx.doi.org/10.1016/j.ijsolstr.2010.11.028.

Becker, R., Smelser, R.E., Richmond, O., Appleby, E.J., 1989. The effect of void shape on void growth and ductility in axisymmetric tension tests. Metall. Trans. A 20A (5), 853–861. http://dx.doi.org/10.1007/BF02651652.

Benzerga, A.A., Leblond, J.B., 2010. Ductile fracture by void growth to coalescence. Adv. Appl. Mech. 44, 169–305. http://dx.doi.org/10.1016/S0065-2156(10)44003-X.

Benzerga, A.A., Leblond, J.B., Needleman, A., Tvergaard, V., 2016. Ductile failure modeling. Int. J. Fract. 201, 29–80. http://dx.doi.org/10.1007/s10704-016-0142-6.

Benzerga, A.A., Surovik, D., Keralavarma, S.M., 2012. On the path-dependence of the fracture locus in ductile materials - analysis. Int. J. Plast. 37, 157–170. http://dx.doi.org/10.1016/j.ijplas.2012.05.003.

Bomarito, G., Warner, D., 2015. Micromechanical investigation of ductile failure in Al 5083-H116 via 3D unit cell modeling. J. Mech. Phys. Solids 74, 97–110. http://dx.doi.org/10.1016/j.jmps.2014.10.007.

Bomarito, G., Warner, D., 2017. Predicting the ductile failure of Al5083-H116 specimens with a mechanistic model and no free fitting parameters. Int. J. Solids Struct. 112, 25–34. http://dx.doi.org/10.1016/j.ijsolstr.2017.02.025.

Brünig, M., Gerke, S., Hagenbrock, V., 2013. Micro-mechanical studies on the effect of the stress triaxiality and the Lode parameter on ductile damage. Int. J. Plast. 50, 49–65. http://dx.doi.org/10.1016/j.ijplas.2013.03.012.

Cadet, C., Besson, J., Flouriot, S., Forest, S., Kerfriden, P., de Rancourt, V., 2021. Ductile fracture of materials with randomly distributed voids. Int. J. Fract. 230 (1), 193–223. http://dx.doi.org/10.1007/s10704-021-00562-7.

Çelik, Ş., Andersen, R.G., Tekoğlu, C., Nielsen, K.L., 2021. On the dependence of crack surface morphology and energy dissipation on microstructure in ductile plate tearing. Int. J. Fract. 230, 115–132. http://dx.doi.org/10.1007/s10704-020-00513-8.

Cheng, L., Guo, T., 2007. Void interaction and coalescence in polymeric materials. Int. J. Solids Struct. 44 (6), 1787–1808. http://dx.doi.org/10.1016/j.ijsolstr.2006.08.007.

Clausing, D.P., 1970. Effect of plastic strain state on ductility and toughness. Int. J. Fract. Mech. 6, 71–85. http://dx.doi.org/10.1007/BF00183662.

Cockroft, M.G., Latham, D.J., 1968. Ductility and the workability of metals. J. Inst. Met. 96, 33–39.

Dæhli, L.E.B., Børvik, T., Hopperstad, O.S., 2016. Influence of loading path on ductile fracture of tensile specimens made from aluminium alloys. Int. J. Solids Struct. 88–89, 17–34. http://dx.doi.org/10.1016/j.ijsolstr.2016.03.028.

Dæhli, L.E.B., Faleskog, J., Børvik, T., Hopperstad, O.S., 2017a. Unit cell simulations and porous plasticity modelling for strongly anisotropic FCC metals. Eur. J. Mech. A Solids 65, 360–383. http://dx.doi.org/10.1016/j.euromechsol.2017.05.004.

Dæhli, L.E.B., Morin, D., Børvik, T., Benallal, A., Hopperstad, O.S., 2020. A numerical study on ductile failure of porous ductile solids with rate-dependent matrix behavior. J. Appl. Mech. 87 (3), 1–12. http://dx.doi.org/10.1115/1.4045524, URL: https://asmedigitalcollection.asme.org/appliedmechanics/article/doi/10.1115/1.4045524/1069585/A-Numerical-Study-on-Ductile-Failure-of-Porous.

Dæhli, L.E.B., Morin, D., Børvik, T., Hopperstad, O.S., 2017b. Influence of yield surface curvature on the macroscopic yielding and ductile failure of isotropic porous plastic materials. J. Mech. Phys. Solids 107, 253–283. http://dx.doi.org/10.1016/j.jmps.2017.07.009.

Dæhli, L.E.B., Morin, D., Børvik, T., Hopperstad, O.S., 2018. A Lode-dependent Gurson model motivated by unit cell analyses. Eng. Fract. Mech. 190, 299–318. http://dx.doi.org/10.1016/j.engfracmech.2017.12.023, URL: https://linkinghub.elsevier.com/retrieve/pii/S0013794417306872.

Dahl, J., Nielsen, K.L., Tvergaard, V., 2012. Effect of contact conditions on void coalescence at low stress triaxiality shearing. J. Appl. Mech. 79 (2), 021003. http://dx.doi.org/10.1115/1.4005565.

Dunand, M., Mohr, D., 2014. Effect of lode parameter on plastic flow localization after proportional loading at low stress triaxialities. J. Mech. Phys. Solids 66 (1), 133–153. http://dx.doi.org/10.1016/j.jmps.2014.01.008.

Faleskog, J., Gao, X., Shih, C.F., 1998. Cell model for nonlinear fracture analysis – I. Micromechanics calibration. Int. J. Fract. 89 (4), 355–373. http://dx.doi.org/10.1023/A:1007421420901.

Frodal, B.H., Dæhli, L.E.B., Børvik, T., Hopperstad, O.S., 2019. Modelling and simulation of ductile failure in textured aluminium alloys subjected to compression-tension loading. Int. J. Plast. 118 (7491), 36–69. http://dx.doi.org/10.1016/j.ijplas.2019.01.008, URL: https://linkinghub.elsevier.com/retrieve/pii/S0749641918305904.

Gao, X., Kim, J., 2006. Modeling of ductile fracture: Significance of void coalescence. Int. J. Solids Struct. 43, 6277–6293. http://dx.doi.org/10.1016/j.ijsolstr.2005.08.008.

Gao, X., Zhang, G., Roe, C., 2010. A study on the effect of the stress state on ductile fracture. Int. J. Damage Mech. 19 (1), 75–94. http://dx.doi.org/10.1177/1056789509101917.

Garrison, W., Moody, N.R., 1987. Ductile fracture. J. Phys. Chem. Solids 48 (11), 1035–1074. http://dx.doi.org/10.1016/0022-3697(87)90118-1.

Guo, T.F., Wong, W.H., 2018. Void-sheet analysis on macroscopic strain localization and void coalescence. J. Mech. Phys. Solids 118, 172–203. http://dx.doi.org/10.1016/j.jmps.2018.05.002.

Gurland, J., Plateau, J., 1963. The mechanism of ductile rupture of metals containing inclusions. Trans. Am. Soc. Met..

Hancock, J.W., Brown, D.K., 1983. On the role of strain and stress state in ductile failure. J. Mech. Phys. Solids 31, 1–24. http://dx.doi.org/10.1016/0022-5096(83)90017-0.

Johnson, G.R., Cook, W.a., 1985. Fracture characteristic of three metals subjected to various strains, strain rates, temperatures and pressures. Eng. Fract. Mech. 21, 31–48.

Keralavarma, S.M., 2017. A multi-surface plasticity model for ductile fracture simulations. J. Mech. Phys. Solids 103, 100–120. http://dx.doi.org/10.1016/j.jmps.2017.03.005.

Keralavarma, S.M., Hoelscher, S., Benzerga, A.A., 2011. Void growth and coalescence in anisotropic plastic solids. Int. J. Solids Struct. 48, 1696–1710. http://dx.doi.org/10.1016/j.ijsolstr.2011.02.020.

Kim, J., Gao, X., Srivatsan, T.S., 2004. Modeling of void growth in ductile solids: Effects of stress triaxiality and initial porosity. Eng. Fract. Mech. 71, 379–400. http://dx.doi.org/10.1016/S0013-7944(03)00114-0.

Koplik, J., Needleman, A., 1988. Void growth and coalescence in porous plastic solids. Int. J. Solids Struct. 24 (8), 835–853. http://dx.doi.org/10.1016/0020-7683(88)90051-0.

Kristoffersen, M., Børvik, T., Hopperstad, O.S., 2016. Using unit cell simulations to investigate fracture due to compression-tension loading. Eng. Fract. Mech. 162, 269–289. http://dx.doi.org/10.1016/j.engfracmech.2016.04.044.

Kuna, M., Sun, D.Z., 1996. Three-dimensional cell model analyses of void growth in ductile materials. Int. J. Fract. 81, 235–258. http://dx.doi.org/10.1007/BF00039573.

Leblond, J.B., Mottet, G., 2008. A theoretical approach of strain localization within thin planar bands in porous ductile materials. C. R. - Mec. 336 (1–2), 176–189. http://dx.doi.org/10.1016/j.crme.2007.11.008.

Lecarme, L., Tekoğlu, C., Pardoen, T., 2011. Void growth and coalescence in ductile solids with stage III and stage IV strain hardening. Int. J. Plast. 27 (8), 1203–1223. http://dx.doi.org/10.1016/j.ijplas.2011.01.004, URL: https://www.sciencedirect.com/science/article/pii/S0749641911000052.

Lin, R.C., Steglich, D., Brocks, W., Betten, J., 2006. Performing RVE calculations under constant stress triaxiality for monotonous and cyclic loading. Internat. J. Numer. Methods Engrg. 66, 1331–1360. http://dx.doi.org/10.1002/nme.1600.

Liu, Z.G., Wong, W.H., Guo, T.F., 2016. Void behaviors from low to high triaxialities: Transition from void collapse to void coalescence. Int. J. Plast. 84, 183–202. http://dx.doi.org/10.1016/j.ijplas.2016.05.008.

Luo, T., Gao, X., 2018. On the prediction of ductile fracture by void coalescence and strain localization. J. Mech. Phys. Solids 113, 82–104. http://dx.doi.org/10.1016/j.jmps.2018.02.002, URL: https://linkinghub.elsevier.com/retrieve/pii/S0022509617303502.

Mackenzie, A., Hancock, J., Brown, D., 1977. On the influence of state of stress on ductile failure initiation in high strength steels. Eng. Fract. Mech. 9 (1), 167–188. http://dx.doi.org/10.1016/0013-7944(77)90062-5.

Maire, E., Zhou, S., Adrien, J., Dimichiel, M., 2011. Damage quantification in aluminium alloys using in situ tensile tests in X-ray tomography. Eng. Fract. Mech. 78, 2679–2690. http://dx.doi.org/10.1016/j.engfracmech.2011.07.004.

Mear, M.E., Hutchinson, J.W., 1985. Influence of yield surface curvature on flow localization in dilatant plasticity. Mech. Mater. 4, 395–407.
Morgeneyer, T.F., Khadyko, M., Buljac, A., Helfen, L., Hild, F., Benallal, A., Børvik, T., Hopperstad, O.S., 2021. On crystallographic aspects of heterogeneous plastic flow during ductile tearing: 3D measurements and crystal plasticity simulations for AA7075-T651. Int. J. Plast. 144 (May), 103028. http://dx.doi.org/10.1016/j.ijplas.2021.103028.
Morgeneyer, T.F., Taillandier-Thomas, T., Buljac, A., Helfen, L., Hild, F., 2016. On strain and damage interactions during tearing: 3D in situ measurements and simulations for a ductile alloy (AA2139-T3). J. Mech. Phys. Solids 96, 550–571. http://dx.doi.org/10.1016/j.jmps.2016.07.012.
Morgeneyer, T.F., Taillandier-Thomas, T., Helfen, L., Baumbach, T., Sinclair, I., Roux, S., Hild, F., 2014. In situ 3-D observation of early strain localization during failure of thin Al alloy (2198) sheet. Acta Mater. 69, 78–91. http://dx.doi.org/10.1016/j.actamat.2014.01.033.
Morin, D., Dæhli, L.E.B., Børvik, T., Benallal, A., Hopperstad, O.S., 2019. Numerical study of ductile failure under non-proportional loading. Eur. J. Mech. A Solids 74 (7491), 221–241. http://dx.doi.org/10.1016/j.euromechsol.2018.11.001, URL: https://linkinghub.elsevier.com/retrieve/pii/S0997753818307733.
Morin, D., Hopperstad, O.S., Benallal, A., 2018. On the description of ductile fracture in metals by the strain localization theory. Int. J. Fract. 209 (1–2), 27–51. http://dx.doi.org/10.1007/s10704-017-0236-9, URL: http://link.springer.com/10.1007/s10704-017-0236-9.
Needleman, A., 1972. Void growth in an elastic-plastic medium. J. Appl. Mech. 39, 964–970. http://dx.doi.org/10.1115/1.3422899.
Needleman, A., Rice, J., 1978. Limits to ductililty set by plastic flow localization. In: Koistinen, D.P., Wang, N.-M. (Eds.), Mechanics of Sheet Metal Forming: Material Behavior and Deformation Analysis. Springer US, Boston, MA, pp. 237 —- 265. http://dx.doi.org/10.1007/978-1-4613-2880-3_10.
Needleman, A., Tvergaard, V., 1992. Analyses of plastic flow localization in metals. Appl. Mech. Rev. 45 (3), S3–S18. http://dx.doi.org/10.1115/1.3121390.
Nielsen, K.L., Dahl, J., Tvergaard, V., 2012. Collapse and coalescence of spherical voids subject to intense shearing: studied in full 3D. Int. J. Fract. 177 (2), 97–108. http://dx.doi.org/10.1007/s10704-012-9757-4.
Noell, P.J., Carroll, J.D., Boyce, B.L., 2018. The mechanisms of ductile rupture. Acta Mater. 161, 83–98. http://dx.doi.org/10.1016/j.actamat.2018.09.006.
Perrin, G., Leblond, J.B., 1993. Rudnicki and rice's analysis of strain localization revisited. J. Appl. Mech. 60, 842–846. http://dx.doi.org/10.1115/1.2900992.
Pineau, A., Benzerga, A., Pardoen, T., 2016. Failure of metals I – Brittle and ductile fracture. Acta Mater. 107, 424–483. http://dx.doi.org/10.1016/j.actamat.2015.12.034, URL: https://linkinghub.elsevier.com/retrieve/pii/S1359645415301403.
Reboul, J., Srivastava, A., Osovski, S., Vadillo, G., 2020. Influence of strain rate sensitivity on localization and void coalescence. Int. J. Plast. 125 (September 2019), 265–279. http://dx.doi.org/10.1016/j.ijplas.2019.09.007.
Rice, J.R., 1976. The localization of plastic deformation. In: Proceedings of the 14th International Congress on Theoretical and Applied Mechanics, Vol. 1. pp. 207–220.
Rogers, H.C., 1960. The tensile fracture of ductile metals. Trans. Metall. Soc. AIME 218 (3), 498–506.
Rudnicki, J.W., Rice, J.R., 1975. Conditions for the localization of deformation in pressure-sensitive dilatant materials. J. Mech. Phys. Solids 23 (1970), 371–394.
Scheyvaerts, F., Onck, P., Tekoğlu, C., Pardoen, T., 2011. The growth and coalescence of ellipsoidal voids in plane strain under combined shear and tension. J. Mech. Phys. Solids 59 (2), 373–397. http://dx.doi.org/10.1016/j.jmps.2010.10.003, URL: https://www.sciencedirect.com/science/article/pii/S0022509610002061.
Shinohara, Y., Madi, Y., Besson, J., 2016. Anisotropic ductile failure of a high-strength line pipe steel. Int. J. Fract. 197, 127–145. http://dx.doi.org/10.1007/s10704-015-0054-x.
Søvik, O.P., Thaulow, C., 1997. Growth of spheroidal voids in elastic-plastic solids. Fatigue Fract. Eng. Mater. Struct. 20, 1731–1744. http://dx.doi.org/10.1111/j.1460-2695.1997.tb01525.x.
Steglich, D., Brocks, W., Heerens, J., Pardoen, T., 2008. Anisotropic ductile fracture of Al 2024 alloys. Eng. Fract. Mech. 75, 3692–3706. http://dx.doi.org/10.1016/j.engfracmech.2007.04.008.
Steglich, D., Wafai, H., Besson, J., 2010. Interaction between anisotropic plastic deformation and damage evolution in Al 2198 sheet metal. Eng. Fract. Mech. 77 (17), 3501–3518. http://dx.doi.org/10.1016/j.engfracmech.2010.08.021.
Tekoğlu, C., Nielsen, K., 2019. Effect of damage-related microstructural parameters on plate tearing at steady state. Eur. J. Mech. A Solids 77, 103818.
Tekoğlu, C., 2014. Representative volume element calculations under constant stress triaxiality, Lode parameter, and shear ratio. Int. J. Solids Struct. 51 (25–26), 4544–4553. http://dx.doi.org/10.1016/j.ijsolstr.2014.09.001.
Tekoğlu, C., Hutchinson, J.W., Pardoen, T., 2015. On localization and void coalescence as a precursor to ductile fracture. Philos. Trans. R. Soc. A 373, 1–19. http://dx.doi.org/10.1098/rsta.2014.0121.
Tekoğlu, C., Pardoen, T., 2010. A micromechanics based damage model for composite materials. Int. J. Plast. 26 (4), 549–569. http://dx.doi.org/10.1016/j.ijplas.2009.09.002.
Thomesen, S., Hopperstad, O.S., Børvik, T., 2021. Anisotropic plasticity and fracture of three 6000-series aluminum alloys. Metals 11 (4), 557. http://dx.doi.org/10.3390/met11040557.
Thomson, R.D., Hancock, J.W., 1984. Ductile failure by void nucleation, growth and coalescence. Int. J. Fract. 26 (2), 99–112. http://dx.doi.org/10.1007/BF01157547.
Tipper, C.F., 1949. The fracture of metals. Metallurgia 39 (231), 133–137.
Tvergaard, V., 1989. Numerical study of localization in a void-sheet. Int. J. Solids Struct. 25 (10), 1143–1156. http://dx.doi.org/10.1016/0020-7683(89)90073-5.
Tvergaard, V., 2012. Effect of stress-state and spacing on voids in a shear-field. Int. J. Solids Struct. 49, 3047–3054. http://dx.doi.org/10.1016/j.ijsolstr.2012.06.008.
Tvergaard, V., 2015. Study of localization in a void-sheet under stress states near pure shear. Int. J. Solids Struct. 75–76, 134–142. http://dx.doi.org/10.1016/j.ijsolstr.2015.08.008.
Tvergaard, V., Legarth, B.N., 2020. 3D study of plastic flow localization at a void-sheet. Int. J. Mech. Sci. 173 (January), 105426. http://dx.doi.org/10.1016/j.ijmecsci.2020.105426, URL: https://linkinghub.elsevier.com/retrieve/pii/S0020740319343838.
Vishwakarma, V., Keralavarma, S.M., 2019. Micromechanical modeling and simulation of the loading path dependence of ductile failure by void growth to coalescence. Int. J. Solids Struct. 166, 135–153. http://dx.doi.org/10.1016/j.ijsolstr.2019.02.015.
Weck, A., Wilkinson, D.S., Maire, E., 2008. Observation of void nucleation, growth and coalescence in a model metal matrix composite using X-ray tomography. Mater. Sci. Eng. A 488 (1–2), 435–445. http://dx.doi.org/10.1016/j.msea.2007.11.050.
Wong, W.H., Guo, T.F., 2015. On the energetics of tensile and shear void coalescences. J. Mech. Phys. Solids 82, 259–286. http://dx.doi.org/10.1016/j.jmps.2015.05.013.
Xiao, Y., Nielsen, K.L., Niordson, C.F., 2021. Size effect on void coalescence under intense shear. Eur. J. Mech. A Solids 90 (November 2020), 104329. http://dx.doi.org/10.1016/j.euromechsol.2021.104329.
Yamamoto, H., 1978. Conditions for shear localization in the ductile fracture of void-containing materials. Int. J. Fract. 14, 347–365. http://dx.doi.org/10.1007/BF00015989.
Yerra, S., Tekoğlu, C., Scheyvaerts, F., Delannay, L., Van Houtte, P., Pardoen, T., 2010. Void growth and coalescence in single crystals. Int. J. Solids Struct. 47 (7), 1016–1029. http://dx.doi.org/10.1016/j.ijsolstr.2009.12.019, URL: https://www.sciencedirect.com/science/article/pii/S0020768309004909.
Yu, H., Olsen, J.S., He, J., Zhang, Z., 2016. Effects of loading path on the fracture loci in a 3D space. Eng. Fract. Mech. 151, 22–36. http://dx.doi.org/10.1016/j.engfracmech.2015.11.005.
Zhang, K., Bai, J.B., François, D., 2001. Numerical analysis of the influence of the lode parameter on void growth. Int. J. Solids Struct. 38, 5847–5856. http://dx.doi.org/10.1016/S0020-7683(00)00391-7.

Zhang, Z., Skallerud, B., 2010. Void coalescence with and without prestrain history. Int. J. Damage Mech. 19, 153–174. http://dx.doi.org/10.1177/1056789508101919.

Zhu, J.C., Ben Bettaieb, M., Abed-Meraim, F., 2020b. Investigation of the competition between void coalescence and macroscopic strain localization using the periodic homogenization multiscale scheme. J. Mech. Phys. Solids 143, http://dx.doi.org/10.1016/j.jmps.2020.104042.

Zhu, J., Bettaieb, M.B., Abed-Meraim, F., 2020a. Numerical investigation of necking in perforated sheets using the periodic homogenization approach. Int. J. Mech. Sci. 166 (April 2019), http://dx.doi.org/10.1016/j.ijmecsci.2019.105209.

Zhu, Y., Engelhardt, M.D., Kiran, R., 2018. Combined effects of triaxiality, lode parameter and shear stress on void growth and coalescence. Eng. Fract. Mech. 199 (June), 410–437. http://dx.doi.org/10.1016/j.engfracmech.2018.06.008.